

# ~~The Capability Fusion of high spatial-temporal remote sensing imagery Landsat 8 OLI and COCI for hourly monitoring surface morphology of lake ice with high resolution in Chagan Lake of Northeast China~~

5 Qian Yang<sup>1,2</sup>, Xiaoguang Shi<sup>1,2</sup>, Weibang Li<sup>3</sup>Li<sup>1</sup>, Kaishan Song<sup>4</sup>Song<sup>2</sup>, Zhijun Li<sup>3</sup>, Xiaohua Hao<sup>4</sup>, Fei Xie<sup>3</sup>, Nan Lin<sup>3</sup>Lin<sup>1</sup>, Zhidan Wen<sup>4</sup>Wen<sup>2</sup>, Chong Fang<sup>4</sup>Fang<sup>2</sup> and Ge Liu<sup>1</sup>Liu<sup>2,\*</sup>.

<sup>1</sup>Northeast<sup>1</sup> Jilin Jianzhu University, School of Geomatics and Prospecting Engineering, Changchun, 130118, China

<sup>2</sup> Northeast Institute of Geography and Agroecology, Chinese Academy of Sciences, Remote Sensing and Geographic Information Research Center, Changchun, 130102, China

10 <sup>3</sup>Jilin Jianzhu University, School of Geomatics and Prospecting Engineering, Changchun, 130118, China

<sup>3</sup>Dalian<sup>3</sup> Dalian University of Technology, State Key Laboratory of Coastal and Offshore Engineering, Dalian, 116024, China

<sup>4</sup>Northwest<sup>4</sup> Northwest Institute of Eco-Environment and Resources, Chinese Academy of Sciences, Lanzhou, 730000, China

Correspondence to: Ge Liu (liuge@iga.ac.cn)

15 **Abstract.** The surface morphology of lake ice ~~undergoes remarkable~~remarkably changes under the combined influence of thermal and mechanical forces, ~~which has been rarely observed by remote sensing. However, research on the surface morphology of lake ice and its interaction with climate is scarce.~~ A large-scale linear structure has repeatedly appeared on satellite images of Chagan Lake in recent years. ~~We proposed a method to extract linear structure on the lake ice surface. We applied it to high spatial-temporal images merged by~~The Geostationary Ocean Color Imager (GOCI) with a 1-hour revisit and Landsat 8 Operational Land Imager (OLI) with a spatial resolution of 30 m provide the possibility to study the hourly changes ~~in the large-scale linear structure. We merged~~ the Landsat and GOCI images using an enhanced spatial and temporal adaptive reflectance fusion model (ESTARFM-), ~~and extracted the lengths and angles of the linear structure.~~ We monitored the hourly changes in ~~the surface morphology in Chagan Lake during the cold season from November 2018 to March 2019, which were further verified as ice ridges during the field investigation.~~ The average length of the ~~ice ridges during~~linear structure in the completely frozen period was  $21141.57 \pm 68.36$  m. The average azimuth angle was  $335.48^\circ \pm 0.23^\circ$ , ~~nearly~~ perpendicular to the ~~wind domain. Besides wind in winter. Through two field investigations during the two recent cold seasons, we discovered~~ ~~spherical~~verified the linear structure as ice balls along the southwestern coast ridges. The ~~deformation~~evolution of surface morphology is closely ~~related to wind direction, snowfall, and associated with air temperature.~~, wind, and shoreline geometry.

25 **Keywords:** remote sensing, lake ice, GOCI, surface morphology, wind, ESTARFM

设置了格式: 字体: 宋体

设置了格式: 字体颜色: 自动设置

## 1 Introduction

The lake ice is one of the Essential Climate Variables in the cryosphere (Bojinski et al., 2014), which is closely associated with the lake environment, ecological regulation, public transportation, and ice activities safety (Hampton et al., 2017; Magnuson et al., 2000; Leppäranta, 2015; Brown and Duguay, 2010; Arp et al., 2020). Shorter ice cover duration and thinner ice thickness have been a common trend throughout the world (Ipeç, 2021; Sroce, 2019; Murfitt and Duguay, 2021). Recent work using remote sensing mainly focused on lake ice phenology (Weber et al., 2016; Zhang et al., 2021; Xie et al., 2020; Murfitt and Duguay, 2020; Du et al., 2017), lake ice classification (Tom et al., 2020; Hoekstra et al., 2020), ice thickness (Murfitt et al., 2018b; Kang et al., 2014; Gogineni and Yan, 2015) and ice albedo (Li et al., 2018; Lang et al., 2018). However, the previous work on the surface morphology of lake ice is scarce, i.e., ice ridges and lake ice fracture. The surface morphology is controlled by dynamic processes of lake ice, which have attracted widespread attention from academia and the public. This paper monitored the surface morphology of Chagan Lake, Northeast China, combining high spatial-temporal remote sensing data and field investigation, and explored the potential influence of climate factors.

Lake ice is one of the essential climate variables in the cryosphere (Bojinski et al., 2014) and is closely associated with lake environments, ecological regulation, public transportation, and the safety of human activities (Hampton et al., 2017; Magnuson et al., 2000; Leppäranta, 2015; Brown and Duguay, 2010; Arp et al., 2020). The shortening of ice cover duration and thinning of ice thickness have been common trends throughout the world (IPCC, 2021; IPCC SROCC, 2019; Murfitt and Duguay, 2021). Recent work using remote sensing mainly focused on lake ice phenology (Weber et al., 2016; Zhang et al., 2021; Xie et al., 2020; Murfitt and Duguay, 2020; Du et al., 2017), lake ice classification (Tom et al., 2020; Hoekstra et al., 2020), ice thickness (Murfitt et al., 2018b; Kang et al., 2014; Gogineni and Yan, 2015) and ice albedo (Li et al., 2018; Lang et al., 2018). However, previous work on the surface morphology of lake ice is scarce. The surface morphology, i.e., ice ridges and fractures, is controlled by the dynamic processes of lake ice, which have attracted widespread concern in academia and the public. In this study, we monitored the surface morphology of Chagan Lake in Northeast China by combining high spatial-temporal remote sensing data and the results of field investigations and explored the potential influences of climate factors.

Satellite remote sensing is macroscopic, multi-source, and wide-range and has been successfully applied in the global remote sensing monitoring of lake ice (Murfitt and Duguay, 2021; Doernhoefer and Oppelt, 2016; Du et al., 2019). (Murfitt and Duguay, 2021; Doernhoefer and Oppelt, 2016; Du et al., 2019). Visible light and multispectral data were first used to monitor lake ice monitoring-based on the spectral difference between ice and water, but, however, the best period for monitoring to monitor lake ice changes is easily prone to be missed due to the influences of clouds, fog, and light (Howell et al., 2009; Cai et al., 2019; Yang et al., 2019; Qi et al., 2020). (Howell et al., 2009; Cai et al., 2019; Yang et al., 2019; Qi et al., 2020). Active microwave data are used to identify the presence of ice through the differences in the backscatter of water and ice, while passive microwave data are through the differences in bright temperature (Cai et al., 2017). (Cai et al., 2017). Microwave remote sensing can penetrate the dry snow on the surface of lake ice surface to, and observe the internal structure and stratification of lake ice (Jones et al., 2013). from the early stage of qualitative differentiation between ground ice and

设置了格式: 字体颜色: 自动设置

设置了格式: 字体颜色: 自动设置

floating ice to ~~the~~ quantitative inversion of ~~lake ice~~ the phenology and thickness (Ke et al., 2013; Jeffries et al., 2013; Howell et al., 2009; Kang et al., 2014) of lake ice (Ke et al., 2013; Jeffries et al., 2013; Howell et al., 2009; Kang et al., 2014). Although the temporal resolution of ~~the~~ active microwave remote sensing data has been improved from 30 days (ERS) to daily return visits (Radasat-2), ~~the~~ optimized technique is too expensive and more suitable for case studies ~~for~~ of small or medium lakes (Murfit et al., 2018a; Geldsetzer et al., 2010) (Murfit et al., 2018; Geldsetzer et al., 2010). With high temporal resolution and ~~time-series~~ temporal coverage, passive remote sensing data can detect ice ~~cover~~ covers under all weather conditions and ~~is~~ are limited by their low spatial resolution and significant mixed image effects. Thus, passive remote sensing is more suitable for monitoring large-scale lake ice monitoring (Du et al., 2017; Qiu et al., 2018). In summary, (Du et al., 2017; Qiu et al., 2018). Although multi-sensor, multi-temporal and multi-spatial resolution source remote sensing image data have been successfully applied is available to monitoring the monitor lake ice. Still processes, single-sensor remote sensing data cannot simultaneously balance clear and achieve accurate remote sensing monitoring with and high frequency.

Lake ice's growth and decay process change very fast, requiring high temporal resolution to capture surface morphology. The satellite sensor with moderate spatial resolution, such as VIIRS and MODIS, can monitor the temporal changes of lake ice daily but fail to reflect spatial details of surface morphology. The satellite sensors with medium spatial resolution, such as Landsat and Sentinel, could provide fine texture, but frequent images are not available to capture the fast changes. The fusion methods consist of unmixing, weight function, and dictionary-pair learning methods (Sisheber et al., 2022; Zhu et al., 2016). The most common weight function method includes the Spatial and Temporal Adaptive Reflectance Fusion Model (STARFM) (Feng et al., 2006), spatial and temporal adaptive algorithm (STAARCH) (Hilker et al., 2009), enhanced version Enhanced Spatial and Temporal Adaptive Reflectance Fusion Model (ESTARFM) (Zhu et al., 2010), flexible spatiotemporal data fusion (FSDAF) model (Zhu et al., 2016), and so on. Previous studies have proved that these spatial-temporal fusion methods could improve the monitoring abilities of remote sensing for specific applications but fail to monitor the abrupt changes in landscapes and spectral differences. All these models are derived by pairs of coarse and fine resolution, e.g., one pair for STARFM, and two pairs for ESTARFM. ESTARFM performs better than STARFM model in heterogeneous landscapes (Zhu et al., 2010; Knauer et al., 2016; Wang et al., 2021b; Jarhani et al., 2014). STAARCH could require two pairs of bases strictly when monitoring the spatial changes, one before and one after the changes. FSDAF is more robust than the other three methods but has limited detection for the tiny changes (Zhu et al., 2016), which make it difficult to monitor the surface morphology changes. Therefore, we generated fusion images with high spatial-temporal resolution based on ESTARFM model for further exploration.

The growth and decay processes of lake ice change very fast, requiring high temporal resolution to capture surface morphology. Satellite sensors with moderate spatial resolution, such as visible infrared imaging radiometer (VIIRS) and moderate resolution imaging spectroradiometer (MODIS), can monitor the temporal changes in lake ice daily but fail to reflect the spatial details of surface morphology. Satellite sensors with medium spatial resolution, such as Landsat and Sentinel, can provide fine texture but have no frequent images to capture fast changes. Fusion methods include the unmixing method, weight function method, and dictionary-pair learning method (Sisheber et al., 2022; Zhu et al., 2016). The most common weight function method

includes the spatial and temporal adaptive reflectance fusion model (STARFM) (Feng et al., 2006), spatial and temporal adaptive algorithm (STAARCH) (Hilker et al., 2009), enhanced spatial and temporal adaptive reflectance fusion model (ESTARFM) (Zhu et al., 2010), and flexible spatiotemporal data fusion (FSDAF) (Zhu et al., 2016). Previous studies have proved that these spatial-temporal fusion methods can improve the monitoring abilities of remote sensing for specific applications but fail to monitor the abrupt changes in landscapes and spectral differences. All these models are derived by pairs of coarse and fine resolution, e.g., one pair for the STARFM and two pairs for the ESTARFM. The ESTARFM performs better than the STRAFM in heterogeneous landscapes (Zhu et al., 2010; Knauer et al., 2016; Wang et al., 2021b; Jarihani et al., 2014). When monitoring spatial changes, the STAARCH strictly requires two pairs of bases, including one before and one after the changes, which limits its wide application. The FSDAF is more robust than the other three methods but has limitations in detecting tiny changes (Zhu et al., 2016), making it difficult to monitor the changes in surface morphology. Therefore, we generated fusion images with the high spatial-temporal resolution based on the ESTARFM for further exploration.

The evolution of a lake ice season is primarily mainly a thermodynamic process under the influence of wind forcing, water level variations, and influenced by thermal and mechanical forces. The thermal Thermal forces enable the surface to melt and freeze when at the turn of the day and night alternate, and the mechanical strength of wind winds and flow make currents makes the ice bulk move and collide, and then causing water eourse courses, ice ridges, and ice fractures to appear, develop and disappear. Therefore, the surface morphology of lake ice exhibits a periodical spatial-temporal difference periodically, which differs significantly from the flat and smooth surface of lake ice. The horizon horizontal and linear structures structures of lake ice was are monitored by optical satellites for large lakes in Europe, which were and have been explained by ice displacement (Leppäranta, 2015). The high (Leppäranta, 2015). High-resolution satellite-airborne Synthetic Aperture Radar synthetic aperture radar (SAR) images have been used to monitor sea ice the surface deformation of sea ice, such as ice ridges (Dierking, 2010) (Dierking, 2010). Moreover, airborne aerial platforms, such as unmanned aerial vehicles (UAVs) (Li et al., 2020), airborne radar (Jeffries et al., 2013), and ground-penetrating radar (Gusmeroli and Grosse, 2012), have effectively complemented remote sensing data sources for monitoring to monitor the changes in lake ice morphology, such as Unmanned Aerial Vehicle (UAV) (Li et al., 2020), airborne radar (Jeffries et al., 2013), and ground penetrating radar (Gusmeroli and Grosse, 2012) the morphology of lake ice. The spatial distribution of lake ice the surface morphology presents of lake ice is complex, variable and discontinuous characteristics, which is characterized by highlighting linear features in on remote sensing images. At present, Currently, there are few studies study on the changes in the surface morphology of lake ice and the impact influence factors, so it. It is meaningful to develop a quantitative method to describe the lake ice surface morphology and explore the potential influences.

This study proposed proved the workflow based on ESTARFM fusion capability of high spatial-temporal remote sensing images to monitor surface morphology in a highly dynamic process. The objectives of our work are to (1) propose a reliable method to extract for monitoring the surface morphology of lake ice; (2) monitor the changes in surface morphology for in Chagan Lake using, Northeast China. Our work aimed to (1) generate high spatial-temporal satellite imagery images using Landsat and Geostationary Ocean Color Imager (GOCI); (2) monitor the hourly spatial changes in the surface morphology, including

设置了格式: 字体颜色: 自动设置

设置了格式: 字体颜色: 自动设置

length and angle. of Chagan Lake; (3) explorediscuss the beneficial climate conditions during the formation mechanism of the surface morphology observed from satellite and field investigation. of lake ice.

## 2 Materials

### 2.1 Study area

The As one of the ten largest lakes in China, Chagan Lake basin (124°03'–124°34'E, 45°09'–45°30'N) (Figure 1), one of the ten largest lakes in China, plays an essential role in fisheries, agricultural irrigation, and winter recreation in the surrounding areas (Wen et al., 2020; Wen et al., 2020). The average and maximum water depths are 2.5 and 4.5 meters (Duan et al., 2007; Song et al., 2011), respectively (Duan et al., 2007; Song et al., 2011). The lake has a water area of 252.86329.72 km<sup>2</sup> and a lengthperimeter of 407.28201.03 km from according to Landsat 8 OLI 8 on January 10, 2019. The salinity of lake areawater ranges from 0.31‰ to 0.78‰ (Liu et al., 2020). The catchment of Chagan Lake is characterized by semi-arid and sub-humid continental monsoons with air temperature, precipitation, and evaporation of 5.5°C, 430 mm, and 1496 mm (Song et al., 2011; Duan et al., 2007), respectively (Song et al., 2011). The salinity ranges from 0.31 to 0.78 ‰ (Liu et al., 2020). The recharge sources mainly consist of comprise precipitation, groundwater, and adjacent irrigation discharge (Liu et al., 2019). The bottom of Chagan Lake is relatively flat, the (Liu et al., 2019). Salinized soil is primarily powdery sandy with the type of white calcium alkaline, and salinized soil farmlandsfarmland and grassland pastures are widely distributed in the catchment area. The Chagan Lake is a typical lake with seasonal frozen lake, and the existence of ice cover lasts, and the ice covers exist from November to April each cold season, with the maximum ice thickness ranging from 0.8 to 1.1 meters (Liu et al., 2020; Hao et al., 2021), respectively (Liu et al., 2020; Hao et al., 2021). We conducted two field investigations from on December 30 to 31, 2020, and January 2 to 4, 2022. The goal was to verify the linear structure observed results from remote sensing images. We measured the ice thickness by thicknesses using an electronic digital calliper with a resolution of 0.01 mm. Besides Moreover, we also measured the water depth by depths using a hand-held sonar detector (SpeedTech SM-5) with a resolution of 0.1 meters and compared the difference between autumn depths of fall (September 17, 2021) and winter (January 2 to 4, 2022).

[Figure 1 is added here]

### 2.2 Materials

#### 2.2.1 GOCI

The Geostationary Ocean Color Imager (GOCI) was is the first satellite for detecting ocean colourcolor from a geostationary orbit, which and has been widely applied in deriving the optical, biological, and biogeochemical properties (Ryu et al., 2012; Ryu and Ishizaka, 2012). GOCI (Ryu et al., 2012; Ryu and Ishizaka, 2012). The GOCI data have been available since April 2004, covering about 2500 km × 2500 km<sup>2</sup> around the Korean Peninsula. It has six visible bands range from 412 to 443 and 540 to 555, 660 to 680 nm and two near-infrared bands range from 745 to 865 nm, and Table 1 provides the detail of band information. The GOCI provides eight hourly observations from local times from 8:0030 to 15:0030 local time, with a spatial

设置了格式: 字体颜色: 自动设置

resolution of 500 m. The ~~best~~COCI has the most significant advantage of ~~COCI is the frequent~~high temporal resolution with eight images daily ~~and could, which can~~ offer the details ~~for~~of freeze-up and break-up processes. A total of 96 GOCI images during the cold season ~~offrom~~from 2018- to 2019 were used in this ~~paper-study~~paper-study (Table 2). The atmospheric correction ~~has-been~~carried out ~~was performed~~ by GOCI data processing software (GDPS).

[Table 1 is added here]

[Table 2 is added here]

### 2.2.2 Landsat

The Landsat 8 satellite was launched on February 11, 2013, ~~carrying~~It carries the Operational Land Imager (OLI) and the Thermal Infrared Sensor (TIRS), which have been widely used ~~for to monitor~~to monitor lake and river ice ~~monitoring~~monitoring (Wang et al., 2021; Yang et al., 2020), ~~with the~~(Wang et al., 2021; Yang et al., 2020). The OLI ~~having has~~has nine bands ~~It has, with~~with a spatial resolution of 30 m for Bands 1–7 and Band 9 and a spatial resolution of 15 m for Band 8. It has a temporal resolution of 16 ~~days~~days. ~~Fourd~~Six Landsat images during the cold season ~~offrom~~from 2018- to 2019 were prepared for data fusion with the GOCI. The capture ~~date is~~dates were November 6, 2018, November 22, 2018, December 08, January 25, 2018, February 26, and 2019, March 14, respectively, 2019, and April 15, 2019. The path and row are 119 and 29, respectively. We downloaded the Landsat calibrated surface reflectance Tier 1 collection for Landsat 8\_OLI ('LANDSAT/LC08/C01/T1\_SR') from the Google Earth Engine (GEE) for further work. ~~More details of~~Table 1 compares the band information ~~of on~~of Landsat and GOCI ~~can be~~From it, we found that the band range of Band 3 of the GOCI (480–500 nm) overlapped with that of Band 2 of the Landsat 8 OLI (450–515 nm). The water body had relatively strong reflectance in Figure 5 the blue band (400–480 nm), and the blue band images clearly displayed the linear structure. Therefore, we merged Band 3 of the GOCI and Band 2 of the Landsat 8 OLI and generated the 96 hourly fusion images for further work.

### 2.2.3 Auxiliary data

The cold season is defined from October of the current year to April of next year according to the local climate. The surface temperature of the lake was extracted from MOD11A1 products for each cold season from 2000 to 2021, following the processing procedure of our previous work (Song et al., 2016; Hao et al., 2021). Daily air temperature, precipitation, wind direction, and wind speed of Qian'an station (ID: 50948) were utilized to explain the influence of climate on lake ice from 2010 to 2021. The longitude and latitude of Qian'an are 124.011° E and 44.998° N, with an elevation of 146.3 meters. The climate records are used to explain the lake ice development. A 16-degree angle with an interval of 22.5° was used to indicate the direction of the wind.

The lake ice phenology of the cold season from 2018 to 2019 was extracted from the combined time series of the surface temperature of lake water provided by MOD11A1 and MYD11A1 products (Song et al., 2016; Hao et al., 2021). The freeze-up date is defined as the first day when the surface temperature of lake water is below 0°C in winter; the break-up date is

195 defined as the first day when the surface temperature of lake water is above 0°C in spring. We utilized the daily air temperatures, precipitation, wind directions, and wind speeds of Qian'an station (ID: 50948) to explain the influence of climate on lake ice from 2010 to 2021. Qian'an has a longitude and latitude of 124.011° E and 44.998° N, respectively, with an elevation of 146.3 m. Sixteen directions with an interval of 22.5° were used to describe the wind directions, including north (N), north-northeast (NNE), northeast (NE), east-northeast (ENE), east (E), east-southeast (ESE), southeast (SE), south-southeast (SSE), south (S), south-southwest (SSW), southwest (SW), west-southwest (WSW), west (W), west-northwest (WNW), northwest (NW), and north-northwest (NNW). The climate records were used to explain the relationship between lake ice and climate.

## 200 3 Methods

### 3.1 The framework of methodology

Figure 2 presents the flow chart of our work ~~herein~~. We pre-processed ~~the~~ Landsat 8 OLI and GOCI and prepared the reflectance images of ~~Band 2 of the~~ Landsat ~~band 28~~ OLI and ~~Band 3 of the~~ GOCI ~~band 3~~. Then, we merged ~~the~~ GOCI and Landsat 8 OLI using the ESTARFM ~~model~~ and generated new fusion data with a spatial and temporal resolution of 30 ~~meters~~ m and 1 hour, ~~respectively~~. After that, ~~we identified~~ the geographic location of the linear structure on the ~~surface of~~ lake ice ~~surface was identified~~, and ~~extracted~~ the morphological parameters ~~were extracted~~, including ~~length~~ lengths and ~~angle~~ angles.

[Figure 2 is added here]

### 3.2 The ESTARFM fusion

210 The ~~enhanced spatial and temporal adaptive reflectance fusion model~~ (ESTARFM) ~~was proposed by Zhu et al. (2010) based on the STARFM model, in~~ which ~~used~~ two pairs of Landsat and GOCI images ~~were used~~ to generate ~~the~~ spatial-temporal fusion data. ~~was proposed by Zhu et al. (2010) based on the STARFM~~. Firstly, the coarse GOCI data ~~was~~ were projected and resampled to a fine Landsat image at two known times  $T_{m1}$  and  $T_{m2}$ . Secondly, similar ~~neighbourhood~~ neighborhood pixels were searched ~~by~~ with a moving window by setting spectral differences. Thirdly, ~~we calculated~~ the normalized weight of each similar pixel ~~was calculated by~~ considering the spatial, spectral, and temporal differences. Then, the coarse GOCI values were transferred to fine Landsat data using the pixel-based conversion coefficients ~~from~~ the linear regression. Finally, the ~~coarse GOCI data at the same time were used to calculate the~~ fine fusion data at the predicted time ( $T_p$ ) ~~are calculated by the coarse GOCI data at the same time, which are~~ expressed as follows (Liu et al., 2021; Bai et al., 2017; Zhu et al., 2010); (Liu et al., 2021; Bai et al., 2017; Zhu et al., 2010):

设置了格式: 字体颜色: 自动设置

设置了格式: 字体颜色: 自动设置

$$L_b(x_{w/2}, y_{w/2}, T_p) = L_b(x_{w/2}, y_{w/2}, T_k) + \sum_{i=1}^n W_i \times v_i \times (G_b(x_i, y_i, T_p) - G_b(x_i, y_i, T_k)) \quad (k = m, n)$$

$$L_b(x_{w/2}, y_{w/2}, t_p) = T_m \times L_{bm}(x_{w/2}, y_{w/2}, t_p) + T_n \times L_{bn}(x_{w/2}, y_{w/2}, t_p) \quad (1)$$

Where  $L_k$  and  $G_b$  represent the  $(x_{w/2}, y_{w/2}, t_p)$  is the final predicted fine-resolution reflectance of MODIS and GOCI images in-band  $b$ ,  $w$  stands for the prediction time  $t_p$ ;  $w$  represents the size of the moving window-size, and the corresponding center is  $(x_{w/2}, y_{w/2})$ ;  $W_i$  is the  $(x_{w/2}, y_{w/2})$ ;  $L_{bk}(x_{w/2}, y_{w/2}, t_p)$  is the fine-resolution reflectance at  $t_k$  ( $k = m$  or  $n$ ) at the base date;  $T_k$  is the time weight of  $a$ , calculated from the magnitude of the detected change in the reflectance of the coarse spatial resolution image between  $t_m$  and  $t_p$  and the prediction moment  $t_p$ :

$$T_k = \frac{1 / \left| \sum_{j=1}^w \sum_{i=1}^w C(x_j, y_i, t_k) - \sum_{j=1}^w \sum_{i=1}^w C(x_j, y_i, t_p) \right|}{\sum_{k=m,n} \left( 1 / \left| \sum_{j=1}^w \sum_{i=1}^w C(x_j, y_i, t_k) - \sum_{j=1}^w \sum_{i=1}^w C(x_j, y_i, t_p) \right| \right)}, \quad (k = m, n) \quad (2)$$

where  $C(x_j, y_i, t_k)$  and  $C(x_j, y_i, t_p)$  denote the image element values of similar pixel contributing to the predicted pixel;  $v_i$  is the conversion coefficients;  $T_k$  is the known time, including  $T_m$  and  $T_n$ , image elements  $(x_j, y_i)$  within the moving window of the coarse spatial resolution image at the reference moment  $t_k$  and prediction moment  $t_p$ , respectively.

### 3.3 The extraction of length and angle for quantitative analysis of linear structures

The In the beginning, the Landsat-GOCI fused fusion images were transformed into binary images. The We extracted the original linear network was extracted by the method of Canny edge detection algorithm; (Canny, 1986) and then conducted edge detection was carried out to remove the outer boundaries (Canny, 1986). The morphological processing, including opening, filling, and eroding sequentially, was implemented for the inner part of the linear network, including opening, filling, and eroding sequentially. Then, we divided the linear structure was derived from the largest connected domain of inner parts into two paths, and the linear network without boundaries, and the length is calculated by the shortest path was considered the final length of the largest connected domain. We connected the northmost and southmost ends into a straight line. The angle was determined as the north-south connection line and the north followed the definition of wind direction along the clockwise direction above. We compared the auto-extraction and visual interpretation in our previous work (Hao et al., 2021). Regarding (Hao et al., 2021). The  $R^2$  values of the length and angle of linear structures, 0.96 and 0.98, and proved the good performance of auto-extraction performed well with an  $R^2$  value of 0.96 and 0.98, respectively algorithm.

域代码已更改

设置了格式

设置了格式; 字体: 倾斜, 非上标/下标

设置了格式

设置了格式

设置了格式

设置了格式

设置了格式; 字体: 倾斜

设置了格式

域代码已更改

设置了格式

设置了格式

设置了格式; 字体颜色: 自动设置

设置了格式; 字体颜色: 自动设置



## 4 Results

### 4.1 The performance of ESTARFM model

We predicted the fine images from two pairs of fine Landsat and coarse GOCI data to fill the data gap caused by the low revisit frequency of the Landsat. The two known pairs of data in the freeze-up process were captured on November 6, 2018, and December 8, 2018, and 53 fine ESTARFM fusion images were predicted from coarse GOCI images. The two known pairs of data of the break-up process were captured on February 26, 2019, and April 15, 2019, and 43 fine ESTARFM fusion images were predicted. Figure 3 displays compares the comparison spatial distribution of the original images and predicted images on November 22, 2018. The two related pairs of Landsat and GOCI were captured on November 6, 2018, and December 8, 2018. The predicted image kept In the predicted images, the texture of the ground objects, which is was maintained, and enlargement figures in Figure 3 (c) and Figure 3 (d) clearly display the distribution of linear structure. The predicted images were well consistent with the original images. We also enlarged part of the linear structure, showing, and indicate a good fusion effect of ESTARFM. Figure 4 illustrates the scatter plots along the 1:1 line of the actual and estimated predicted reflectance values and along the corresponding statistical results 1:1 line. The  $R^2$  had the value of 0.93, which indicated 935, indicating that the predicted image was highly correlated with the actual image. Besides, we compared the reflectance values of original images and predicted images on November 22, 2018. The result showed that the range of estimated The ranges of predicted and actual images was were consistent; the mean of their mean reflectance values was were both  $0.10 \pm 0.03$ . The performance of the ESTARFM results was limited by (1) the limited image pairs available during the cold season from 2018 to 2019; (2) the time lag between the predicted and actual images; (3) the inconsistency of capture time between the predicted images and two pairs of input images (Lu et al., 2019; Liu et al., 2018). Therefore, the ESTARFM fusion images had a good performance and provided can provide reliable materials for further exploration.

[Figure 3 and 4 is added here]

We predicted the fine images from two pairs of fine Landsat and coarse GOCI data to fill the data gap caused by the low revisit frequency of Landsat. The high  $R^2$  between actual and predicted images was 0.935 on November 28, 2018, which proved that the fusion images are consistent with the remote sensing data. Liu (2018) et al. pointed out that when validating the ESTARFM model, a 4 day time lag between fusion and validation results may lead to errors in the analysis of the results. The time lag in our study ranged from 5.5 to 12.5 hours for Landsat and GOCI, and the assumption that the lake ice will not change dramatically in a short period. The performance of ESTARFM results was limited by: (1) Only three image pairs were available during the cold seasons; (2) the time lag between the prediction and verification images; (3) the inconsistency between the predicted time and two input pairs (Lu et al., 2019; Liu et al., 2018). The ESARFAM model predicted the reflectance using a linear model and assumes that the reflectance changes steadily during the fusion process (Liu et al., 2018). These limitations need to be considered in our future work.

设置了格式: 字体颜色: 自动设置

## 4.2 The changes in surface morphology

We extracted the surface morphology of Chagan Lake from 96 fusion images during the cold season ~~of~~ from 2018- to 2019.

Figure 5 displays ~~the~~ spatial changes ~~of in the~~ linear structure ~~of~~ Landsat images ~~during in~~ the freeze-up and break-up ~~process~~. ~~Figure S3~~ processes. ~~Figures A1~~ and ~~Figure S4~~ presented ~~A2~~ present the original images ~~from of the~~ GOCI with a resolution of 500 ~~meters~~ m, the fusion images ~~from of the~~ Landsat and GOCI with a spatial resolution of 30 ~~meters~~ m, the network structure of surface morphology, and the ~~surface morphology during~~ linear structure in the freeze-up and break-up ~~process~~, which ~~provide~~ processes, ~~providing~~ more details of the extraction process. The linear structure ~~on image~~ appeared on images from

southeast to northwest, lasting from November 22, 2018, to November 30, 2018. The linear structure disappeared from the northwest to southeast, lasting from March 15 to March 24, 2019, 2019, to March 24, 2019. Figure 6 shows the average daily lengths of ice ridges based on the Landsat and GOCI remote sensing data. We monitored the growth and recession process of the linear structure via 96 Landsat-GOCI fusion images and monitored the stable process via four Landsat images. The growth stage lasted for 9 days, from November 22, 2018, to November 30, 2018. The ice ridges had a length range of 5211.17–18042.15 m and an average value of  $12680.32 \pm 4472.37$  m, extending from southeast to northwest. The azimuth angles of the ice ridges in the growth stage ranged from  $331.54^\circ$  to  $338.17^\circ$ , with an average value of  $334.38^\circ \pm 2.08^\circ$ . The lengths in the stable process ranged from 21052.78 m to 21227.53 m with an average value of  $21141.57 \pm 68.26$  m, and the angles changed from  $335.15^\circ$  to  $335.77^\circ$  with an average value of  $335.48 \pm 0.20^\circ$ . The recession stage lasted for 10 days, from March 15, 2019, to March 24, 2019. The ice ridges had a length range of 19178.18–5924.03 m and an average value of  $13288.59 \pm 4907.89$  m, disappearing from northwest to southeast. The azimuth angles of the ice ridges in the recession stage ranged from  $329.84^\circ$  to  $336.16^\circ$ , with an average value of  $332.90^\circ \pm 2.54^\circ$ . The changing rates in the growth and recession stages were 1425.66 and 1325.42 m per day, respectively, indicating that growth was slightly faster than recession. The large-scale fracture structure extending from northwest to southeast ~~that~~ repeatedly appeared on Landsat images since 1986, which has been reported in our previous work (Hao et al., 2021); (Hao et al., 2021).

[Figure 5 is added here]

Figure 6 shows the average daily length of ice ridges from Landsat and GOCI remote sensing data. It can be seen that the ice ridge changes in the winter of 2018-2019 can be divided into three processes, including the growth process, stable process, and recession process. The growth stages lasted from November 22 to November 30, a total of 9 days. The length of the ice ridge changed from 5211.17 meters to 18042.15 meters with an average value of  $12680.32 \pm 4472.37$  meters, extending from the southeast to the northwest. The average azimuth angle of the ice ridges during the growth process was  $334.38^\circ \pm 2.08^\circ$  ranging from  $331.54^\circ$  to  $338.17^\circ$ . The recession lasted from March 15, 2019, to March 24, 2019, a total of 10 days. The length of the ice ridge changed from 19178.18 meters to 5924.03 meters with an average value of  $13288.59 \pm 4907.89$  meters, disappearing from northwest to southeast. The average azimuth angle of the ice ridges during the recession process was  $332.90^\circ \pm 2.54^\circ$  ranging from  $329.84^\circ$  to  $336.16^\circ$ . The changing growth and recession process rate were 1425.66 and 1325.42 meters per day, which suggests the growth is slightly faster than the recession process.

设置了格式: 字体颜色: 自动设置

设置了格式: 字体颜色: 自动设置

[Figure 6 is added here]

### 4.3 The field investigation

The lake ice process is governed by the complex interaction of hydraulics, thermodynamics, and mechanics. The heat loss caused by decreasing air temperature exceeds the heat gained from the surface water in the late autumn and early winter. When the water temperature falls below the freezing point, the cooling water provides a beneficial condition for ice crystals. Then the volume of lake ice expands and the amount increases, followed by ice formation. The average freeze-up date of Chagan Lake was November 12 during the 12 recent cold seasons from 2010 to 2022, which has been listed in Table S1 (Hao et al., 2021). Considering the safety of traveling safety on ice, we conducted two thoroughfield investigations during the two recent cold seasons, on from December 30 to 31, 2020, and January 2 to 4, 2022, respectively. We divided the lake area into three regions according to the surface morphology of lake ice. Region 1 was distributed along the linear structures. The surface of lake ice is uneven, and ice fractures and ice ridges were widely distributed. Region 2 was distributed along the northeastern coast, where the Ice and Snow Fishing and Hunting Cultural Tourism Festival of Chagan Lake has been held at the end of December each year. Region 3 covered the southern part of Chagan Lake. The lake ice in Regions 2 and Region 3 was flat and smooth, and snow cover was sporadically distributed. The color of lake ice along the linear structure was distinguished from lake ice in the neighborhood. We infer that the frozen time of linear structure was later than the lake ice in the neighborhood. The difference between ice fractures and ice ridges was the vertical height. Ice ridges were elevated sections formed on the upper and lower surfaces of lake ice, consisting mainly of ridge sails and keels. We located ten sampling points along the linear structure on the satellite images and collected field photos of ice ridges and fractures, as shown in (Figure 1-). We further verified the large-scale fractures on the images as ice ridges. More interesting is that we both discovered ice balls along the southwest coast of Chagan Lake in the two years, as shown in Figure 7. The ice ball piled above the ice surface in the winter of 2020, and the ice was so uneven that the cars had difficulties traveling on the ice surface. However, the ice ball in 2022 was frozen beneath the ice surface, and the surface was relatively smooth.

We also measured the ice thicknesses and water depths of each 16 sampling point, presented in points (Figure 7-). The ice thicknesses in the winter of 2022021 ranged from 437.55 mm to 668.25 mm, with an average value of  $582.24 \pm 58.14$  mm. We divided into three regions: Region 1 was distributed along the ice ridges; Region 2 was distributed along the north-eastern coast; Region 3 covered the southern part of Chagan Lake. The average values ice thicknesses of regions Regions 1, 2, and 3 were 551.58 mm, 547.75 mm, and 645.74 mm, respectively. The average water depths of Regions 1, 2, and 3 were 3.48, 2.99, and 3.00 m, respectively. Among the three regions, the ice thickness Region 2 had the smallest value-average values of ice thickness and water depth. The differences in water depth between summerthe fall of 2021 and winterthe winner of 2021 varied from 0 to 0.2 m with had an average value of  $0.12 \pm 0.05$  m. This indicated that winter's and a maximum value of 0.2 m. The water depth is in winter was lower than summer's, but the differences were not significant enough to explain what we observed from the satellite that in fall, and the decreasing water level also was a cause of lake ice fracturing in winter (Leppäranta, 2015). The ice features first formed in the southeast coast's nearshore area of the

设置了格式: 字体: 宋体

southeast coast, where the water depth was relatively shallower than that in other regions in Figure 7. The ice thickness and water depth showed spatial coherence with the surface morphology, especially with the ice thickness.

[Figure 7 is added here]

#### 4.4 The climate condition

As shown in Figure 8, Lake ice processes are governed by the complex interaction of hydraulics, thermodynamics, and mechanics. The heat loss due to the decreasing air temperature exceeds the heat gained from surface water in late fall and early winter. When the water temperature falls below the freezing point, the cooled water provides a beneficial condition for ice crystals. Then, the volume of lake ice expands, and the amount increases, followed by the formation of ice. We analyzed the wind roses and daily average and maximum wind speeds from November 1, 2018, to April 15, 2019 (Figure 8).

The freeze-up and break-up dates of Chagan Lake in the cold season of 2019 are derived from MODIS LST products were November 14, 2018, and March 22, 2019, respectively. The ice ridges appeared on November 22, 2018, 5 days later than after the freeze-up date; they disappeared on March 24, 2019, 2 days later than and were consistent with the break-up date. The temporal resolution of MODIS LST products is eight days. Domain wind in the growth process was NW, WNW, W, and E, and can explain the time difference. We also found that WSW; the WSW (247.5°) domain wind in the stable process was WNW, WSW, and NNE; the domain wind in the recession process was NW, WNW, and WSW. WNW and WSW direction had a relatively high frequency as the domain wind direction for all three stages. The frequency of WSW in the WSW direction in the growth, stability, and recession stages was 22.22%, 30%, and 14.23% for the growth, stable, and disappearing processes, respectively. The angles between the WSW direction and ice ridges were 87.98°, 86.88°, and 85.4° for the three stages. The nearly perpendicular relationship was consistent with our previous study (Hao et al., 2021). Moreover, the three quartiles of daily average speed were 3.52 m/s, and those (Hao et al., 2021). Our previous used the yearly average values of wind from 2013 and 2020, and the work herein just exploited the wind in the cold season from 2018 to 2019. Besides, the wind speed also contributed to the formation of ice cracks and ridges. The daily average wind speed in the growth process (3.88 m/s) and recession process (was 3.88 m/s and 3.63 m/s), and the average values for the whole cold season were more prominent than the three quartiles. The three quartiles of 2.97 m/s. Both the daily maximum wind speed were 6.92 m/s, and those of in the growth process (7.05 m/s) and recession process (6.86 m/s) were close to the three quartiles: was 3.88 m/s and 3.63 m/s 7.05 m/s and 6.86 m/s, and the average values for the whole cold season were 5.65 m/s. Not only daily average values but also the maximum value was higher than the average level and revealed that the changing processes of ice fractures and ridges require relatively strong action of wind. Therefore, wind speeds and directions played a crucial role in the development of ice ridges.

[Figure 8 is added here]

To explain the existence of ice balls, we checked the changes in air temperature, precipitation, wind speed, and wind direction of Lake Chagan around the freeze-up periods from 2010 to 2021, as shown in Figure 9. The freeze-up dates were provided by

设置了格式: 字体颜色: 自动设置

设置了格式: 字体颜色: 自动设置

设置了格式: 字体颜色: 自动设置

MODIS (Table S1), and we calculated the average values covering one week before and after the freeze-up date. The air temperature in the cold season of 2020 and 2021 was not significantly different from other years, but the precipitation was significantly higher than in other years. The values were 20.9 and 12.5 mm in 2020 and 2021, respectively, and further were considered snowfall because of the air temperature below 0°C. In addition, the average wind speed in these two years is 7.2 and 12.3 m/s, which is significantly higher than the other years. More interestingly, the wind direction of the northeast direction happened during the freeze-up periods for both years, while the southwest wind dominated the other years. We deduced that the northeast wind blew the ice balls to the southwest shore, which created the marvelous geographic landscape we found during the fieldwork. Therefore, the air temperature, snowfall, and wind create favourable conditions for ice ball.

{Figure 9 is added here}

## 5 Discussion

The lake ice ~~experieneed~~experiences different ~~phasestypes~~ phases during the freezing and thawing cycle, including the phases of ice ~~crystalcrystals~~ crystals, frazil ice, nails, pancake ice, and ice layer. The lake ice began to freeze in shallow water areas and expanded to the lake centre until the lake was completely frozen layers (Leppäranta, 2015). Lake ice deformed under the combined influence of thermodynamics and hydrodynamics, resulting in lead, cracks, and ice ridges. The lake ice expanded and ~~contraeted~~expands and contracts as the air temperature ~~roses~~risers and ~~dropped~~drops during the cold ~~season~~seasons. The temperature difference between night and day results in ~~lake ice's~~the thermal expansion and ~~contraets~~contract of lake ice, which differ significantly within a given lake. Furthermore, long and narrow cracks ~~then happened~~are generated and were likely to evolve into ice ridges under the pressure when the lake ice ~~bulked, collided~~bulk, collides, and ~~piled~~piles up. The ~~view ranged~~definitions of lake ice are limited ~~traditional by the view ranges of field measurement and had difficulty identifying the spatial distribution of ice ridges. In this work, we proposed an algorithm to detect the high-lightened measurements, and satellite remote sensing provides a new perspective for surface morphology in a larger-scale observation. The large-scale linear structure based~~has been found on remote sensing images. ~~The recurrent linear structure on a large seale-~~ during the cold season from 2018 to 2019. Similar phenomena have also been found in lakes and reservoirs in Northeast China (Liu et al., 2018b). In our previous work, we used 4 Landsat 8 OLI images to monitor the monthly changes due to the limitation of temporal resolution (Hao et al., 2021). In this study, we took advantage of the hourly revisit of the GOCI and generated 53 and 43 ESTAREM fusion images in the freeze-up and break-up processes, respectively. This makes it possible to explore the linear structure in detail. The recurrent large-scale linear structure was further verified as ice fractures and ice ridges in the fieldwork. The ice ridges were supposed to happen in the area with thinner ice thickness. During the field investigation, we measured the ice thickness along the linear structure. We compared it with the other regions (Figure 7), and the difference of ice thickness is not significant to support this. ~~The spatial scales of ice fractures and ice ridges is a changeling work when considering the data source. The UAV is suitable to monitor the lake ice fractures at small scales (0-100m), and the satellite sensors are suitable to monitor the ice ridges at large scales (10-100 km), both of which required a thorough investigation of ice thickness in~~

设置了格式: 字体颜色: 自动设置

405 ~~Chagan Lake by combining a suitable to monitor the in-situ measurement and remote sensing monitoring horizon changes of the lake ice surface.~~

~~The development of seasonal~~ Besides the thermal forces, the lake ice ~~is~~ fractures and ridges are also a dynamic process, ~~and the~~ under the control of mechanical forces. The wind ~~above ice covers~~ and water currents ~~beneath ice covers~~ force the shift of ice bulk. ~~During~~ (Tan et al., 2012). Wang et al. (2006) compared the machinal changes of leads and ice covers based on modelling results and satellite monitoring (Wang et al., 2006; Leppäranta, 2010) and revealed the influence of winds on the drift of ice.

410 In the freeze-up process, the ~~wind~~winds and water ~~flow~~currents can push the ice toward the shore, preventing ~~the ice~~ ~~cover~~covers from freezing; ~~during~~in the break-up process, the wind ~~could~~can break ~~the ice~~ ~~cover~~covers and accelerate the melting. ~~The lake ice fractures were mainly controlled by thermal forces, and the ice ridges were mainly controlled by mechanical forces.~~ The ice ridges underwent three stages during the cold season of 2018, ~~during 2019, in~~ which the wind ~~direction~~directions and ~~speeds~~speeds exhibited remarkable differences ~~in Figure 8.~~. The ice ridges grew from southeast to

415 northwest with an average direction of  $334.38^\circ$  and decayed from northwest to southeast with an average direction of  $332^\circ$ .

~~The direction of ice ridges is nearly perpendicular to  $-90^\circ$ . The WSW ( $247.5^\circ$ ), which direction frequently happened for~~in all three ~~periods~~stages, revealing the crucial role of ~~wind~~winds in the development of ice ridges. ~~However, more aspects should be considered. More interestingly, the~~The direction of the ice ridges was nearly perpendicular to the WSW direction of ( $247.5^\circ$ ), which followed the principal laws of mechanics. The air temperature created a cold environment for the ice cover to freeze.

420 ~~the wind provided a mechanical force for the ice bulk to shift, and ice ridges and ice fractures formed. In addition, the direction of the ice ridges had a similar shape to the southwest shoreline, and the stable shoreline geometry could explain the recurrent ice ridges with a specific direction, which had been~~was reported in previous studies (Leppäranta, 2015). (Leppäranta, 2015).

~~We also discovered the spherical ice ball in the neighbourhood of the southeast coast, and this rare geographic scenic attracted our interest, which has been reported in Finland, Japan, and so on (Case, 1906; Loewe, 1949; Langlois, 1965; Eisen et al.,~~

425 ~~2003; Kawamura et al., 2009). From Figure 9, the occurrence of ice ball needs to meet the strict requirements of climate conditions together during the frozen process: (1) the air temperature varies up and down the freezing point and can meet the freezing conditions; the temperature cannot be lower than  $-10^\circ\text{C}$ . Otherwise, the ice will directly freeze completely; (2) sufficient snowfall is necessary to provide material sources for the emergence of ice balls, snow and water mixed and frozen together, the final ice balls formed under the continuous washing of wind and waves; (3) wind speed is large enough to push~~

430 ~~the rolling spherical ice to southwest coast only if the wind direction was northeast before freezing, and then ice balls aggerated the nearshore areas (Xie et al., 2022(in Chinese)). During the past decade, only the cold season of 2020 and 2021 could meet all three conditions, and we, fortunately, discovered these ice balls during the field investigation.~~

435 ~~Linear structures are common natural phenomena on the surfaces of sea ice and lake ice and profoundly influence light transfer and ice ecology. Lake ice ridges alter surface roughness and light transfer and contribute to the thickness and volume of ice. People in cold regions have skilfully taken advantage of frozen ice covers for fishing, food storage, and commercial~~

设置了格式: 15, 字体: Arial, 图案: 清除 (白色)

transportation. The capacity and stability of floating ice can be evaluated by the ice thickness and the spatial distribution of ice fractures and ridges (Tan et al., 2012). Generally, 30 cm is the thickness suggested for safe human activities on the ice (Leppäranta, 2015). Ice fractures and ice ridges potentially threaten human activities. In the field investigations, we measured the ice thicknesses along the linear structure when the ice covers were steady. The ice thicknesses along the ice ridges were supposed to be thinner than in other areas (Leppäranta, 2015), but no significant difference in ice thickness had been found in our field measurements. Thus, the surface morphology of lake ice would be a reliable sign of dangerous traveling. Besides, we monitored the horizon changes in lake ice ridges using optical satellite images but ignored the vertical heights of ice ridges, which need to consider in future work.

## 6 Conclusion

We generated high spatial-temporal remote sensing data from the Landsat and GOCI using the ESTARFM, and filled to fill the gap for the fine monitoring of lake ice dynamics in Lake Chagan. We compared the reflectance of the fusion images and the original images on November 22, 2018. The scatter plot was centred around 1:1 with the  $R^2$  value of 0.93, which indicated between the actual images and predicted images is up to 0.935, indicating the predicted images were highly correlated with the actual image. Besides images, Moreover, the predicted image kept consistency of the ground objects' texture consistent with of the ground objects was maintained between the predicted images and the original images. Therefore, the ESTARFM fusion images provided reliable materials for further exploration.

We proposed the automatic extraction and calculated the lengths and the angles of the linear structure on the fusion images in the freeze-up and break-up processes during the cold season from 2018 to 2019. Based on the satellite images, the linear structure experienced growth, stability, and decay-recession stages. The growth lasted nine days, just four days later than the freeze-up date from MODIS; The decay process stage lasted for 9 days ranging from November 22 to November 30, 2018. The recession stage lasted for 10 days, just two days earlier than the break-up date, ranging from March 15 to March 22, 2019. From southeast to northwest, the linear structure was 5211.17 to 18042.15 meters long during growth; from northwest to southwest, it disappeared. The average length of the ice ridges during the fully completely frozen period was  $21141.57 \pm 68.36$  m. The average azimuth angle was  $335.48^\circ \pm 0.23^\circ$ .

We carried out several performed field investigations and verified the linear structure of the ice ridges, along which we also discovered spherical ice balls. The direction of the ice ridges was nearly perpendicular to the southwest wind direction, which is the dominant wind direction with high frequency in winter. The deformation of the surface morphology was related to the meteorological conditions before the freeze-up process, including wind, snowfall, winds and air temperatures. This work demonstrates demonstrated the capability of monitoring large-scale surface morphology using multi-source remote sensing. We need to simulate the flow field using the hydrodynamic model and explore the relationship between the hydrodynamic field has profound implications for traveling safety on ice and ice engineering. We also plan to extend our findings to other large lakes in China and fill the knowledge gap of the surface morphology of the lake ice in the future.

设置了格式: 字体颜色: 自动设置

Appendices:

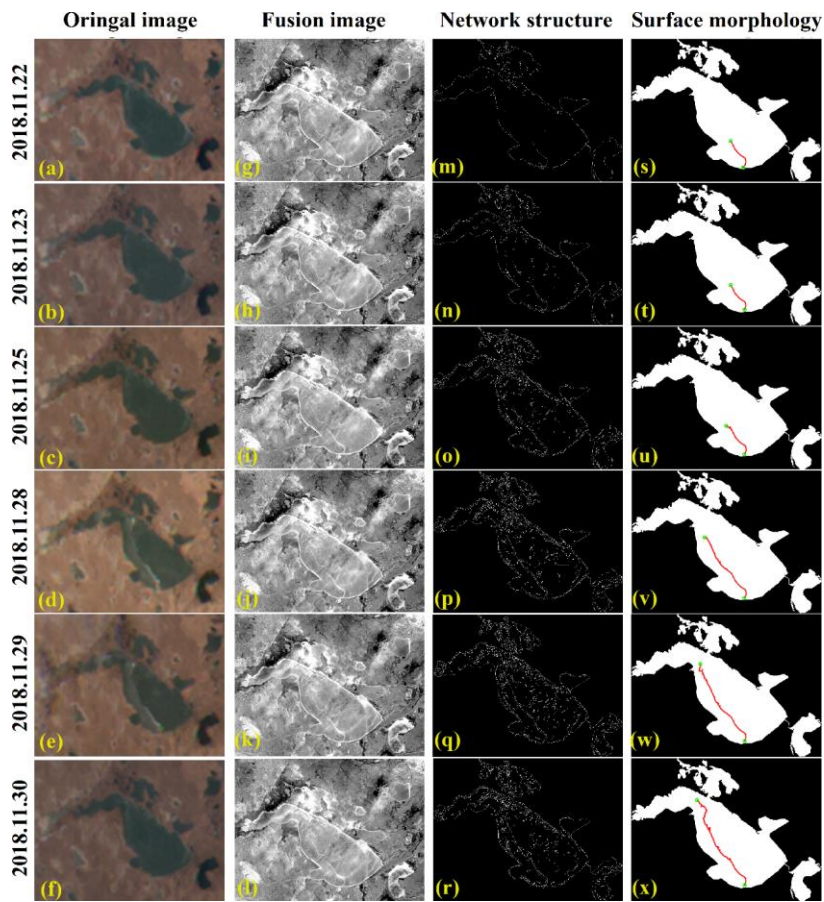
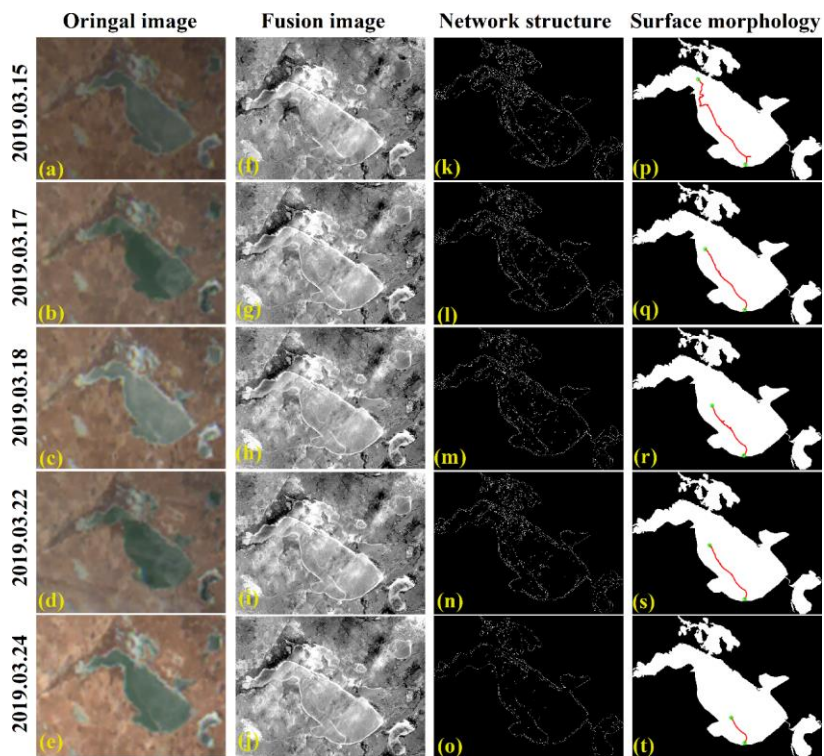


Figure A1 The changes of ice ridges during the freeze-up process from November 22 to November 30, 2019: (a-f) the original images from GOCI; (g-l) the fusion images from Landsat and GOCI; (m-r) the network structure of surface morphology; (s-x) the surface morphology.

470





475 [Figure A2](#) The changes of ice ridges during the break-up process from March 15 to March 24, 2019: (a-e) the original images from GOCI; (f-j) the fusion images from Landsat and GOCI; (k-o) the network structure of surface morphology; (p-t) the surface morphology.

**[Data availability](#)**

All raw data can be provided by the corresponding authors upon request.

480 **[Author contribution:](#)**

[YQ, XF, and LZJ](#) planned the field investigation; [SXG and LWB](#) processed the remote sensing data; [FC and LN](#) analyzed the data; [YQ and SKS](#) wrote the manuscript draft; [HXH, LZJ, WZD, and LG](#) reviewed and edited the manuscript.

## Acknowledgment

The authors would like to thank the KORDI/KOSC for providing GOCI data, the GEE platform for providing MODIS and Landsat data, and the China Meteorological Data Sharing Service System for climate records. Thanks are given to our students Feng Tao, Xuan Li, and Kenan Sun for helping with the field investigation. The anonymous reviewers to improve the quality of this manuscript are greatly appreciated.

## Financial support

This research was jointly supported by the National Natural Science Foundation of China (41971325), the 14th Five-Year Plan of Technical and Social Research Project for Jilin Colleges of China (JKH20210290KJ), the National Natural Science Foundation of China (41971325), and the National Key Research and Development Program of China (2019YFE0197600).

## References

- Arp, C. D., Cherry, J. E., Brown, D., Bondurant, A. C., and Endres, K. L.: Observation-derived ice growth curves show patterns and trends in maximum ice thickness and safe travel duration of Alaskan lakes and rivers, *The Cryosphere Discussions*, 1–35, 2020.
- Bai, L., Cai, J., Liu, Y., Chen, H., Zhang, B., and Huang, L.: Responses of field evapotranspiration to the changes of cropping pattern and groundwater depth in large irrigation district of Yellow River basin, *Agricultural Water Management*, 188, 1–11, 10.1016/j.agwat.2017.03.028, 2017.
- Bojinski, S., Verstraete, M., Peterson, T. C., Riecher, C., Simmons, A., and Zemp, M.: The Concept of Essential Climate Variables in Support of Climate Research, Applications, and Policy, *Bulletin of the American Meteorological Society*, 95, 1431–1443, 10.1175/bams-d-13-00047.1, 2014.
- Brown, L. C. and Duguay, C. R.: The response and role of ice cover in lake climate interactions, *Progress in Physical Geography Earth and Environment*, 34, 671–704, 10.1177/0309133310375653, 2010.
- Cai, Y., Ke, C.-Q., and Duan, Z.: Monitoring ice variations in Qinghai Lake from 1979 to 2016 using passive microwave remote sensing data, *Science of the Total Environment*, 607, 120–131, 10.1016/j.scitotenv.2017.07.027, 2017.
- Cai, Y., Ke, C.-Q., Li, X., Zhang, G., Duan, Z., and Lee, H.: Variations of Lake Ice Phenology on the Tibetan Plateau From 2001 to 2017 Based on MODIS Data, *Journal of Geophysical Research Atmospheres*, 124, 825–843, 10.1029/2018jd028993, 2019.
- Canny, J.: A computational approach to edge detection, *IEEE Transaction on Pattern Analysis and Machine Intelligence*, PAMI-8, 679–698, 1986.
- Case, E. C.: A Peculiar Formation of Shore Ice, *The Journal of Geology*, 14, 134–137, 10.1086/621287, 1906.
- Dierking, W.: Mapping of Different Sea Ice Regimes Using Images From Sentinel-1 and ALOS Synthetic Aperture Radar, *IEEE Transactions on Geoscience and Remote Sensing*, 48, 1045–1058, 10.1109/TGRS.2009.2031806, 2010.
- Doernhoefer, K. and Oppelt, N.: Remote sensing for lake research and monitoring—Recent advances, *Ecological Indicators*, 64, 105–122, 10.1016/j.ecolind.2015.12.009, 2016.
- Du, J., Kimball, J. S., Duguay, C., Kim, Y., and Watts, J. D.: Satellite microwave assessment of Northern Hemisphere lake ice phenology from 2002 to 2015, *Cryosphere*, 11, 47–63, 10.5194/te-11-47-2017, 2017.
- Du, J., Watts, J. D., Jiang, L., Lu, H., Cheng, X., Duguay, C., Farina, M., Qiu, Y., Kim, Y., Kimball, J. S., and Tarolli, P.: Remote Sensing of Environmental Changes in Cold Regions: Methods, Achievements and Challenges, *Remote Sensing*, 11, 10.3390/rs11161952, 2019.
- Duan, H., Zhang, Y., Zhang, B., Song, K., and Wang, Z.: Assessment of chlorophyll a concentration and trophic state for Lake Chagan using Landsat TM and field spectral data, *Environ Monit Assess*, 129, 295–308, 10.1007/s10661-006-9362-y, 2007.

设置了格式: 字体颜色: 自动设置

设置了格式: 字体颜色: 自动设置

- Eisen, O., Freitag, J., Haas, C., Rack, W., Rotschky, G., and Schmitt, J. J. o. G.: Bowling-mermaids; or, How do beach-ice balls form?, 49, 605–606, 2003.
- 525 Feng, G., Masek, J., Schwaller, M., and Hall, F.: On the blending of the Landsat and MODIS surface reflectance: predicting daily Landsat surface reflectance, IEEE Transactions on Geoscience and Remote Sensing, 44, 2207–2218, 10.1109/tgrs.2006.872081, 2006.
- Geldsetzer, T., Sanden, J. v. d., and Brisco, B.: Monitoring lake ice during spring melt using RADARSAT-2 SAR, Canadian Journal of Remote Sensing, 36, S391–S400, 2010.
- 530 Gogineni, P. and Yan, J.-B.: Remote sensing of ice thickness and surface velocity, in: Remote Sensing of the Cryosphere, edited by: Tedesco, M., John Wiley & Sons, Ltd., 2015.
- Gusmeroli, A. and Grosse, G.: Ground penetrating radar detection of subsnow slush on ice-covered lakes in interior Alaska, The Cryosphere, 6, 1435–1443, 10.5194/te-6-1435-2012, 2012.
- 535 Hampton, S. E., Galloway, A. W., Powers, S. M., Ozersky, T., Woo, K. H., Batt, R. D., Labou, S. G., O'Reilly, C. M., Sharma, S., Lottig, N. R., Stanley, E. H., North, R. L., Stockwell, J. D., Adrian, R., Weyhenmeyer, G. A., Arvola, L., Bauleh, H. M., Bertani, I., Bowman, L. L., Jr., Carey, C. C., Catalan, J., Colom-Montero, W., Domine, L. M., Felip, M., Granados, I., Gries, C., Grossart, H. P., Haberman, J., Haldna, M., Hayden, B., Higgins, S. N., Jolley, J. C., Kahilainen, K. K., Kaup, E., Kehoe, M. J., MacIntyre, S., Mackay, A. W., Mariash, H. L., McKay, R. M., Nixdorf, B., Noges, P., Noges, T., Palmer, M., Pierson, D. C., Post, D. M., Pruett, M. J., Rautio, M., Read, J. S., Roberts, S. L., Rueker, J., Sadro, S., Silow, E. A., Smith, D. E., Sterner, R. W., Swann, G. E., Timofeyev, M. A., Toro, M., Twiss, M. R., Vogt, R. J., Watson, S. B., Whiteford, E. J., and Xenopoulos, M. A.: Ecology under lake ice, Ecol Lett, 20, 98–111, 10.1111/ele.12699, 2017.
- 540 Hao, X., Yang, Q., Shi, X., Liu, X., Huang, W., Chen, L., and Ma, Y.: Fractal-Based Retrieval and Potential Driving Factors of Lake Ice Fractures of Chagan Lake, Northeast China Using Landsat Remote Sensing Images, Remote Sensing, 13, 10.3390/rs13214233, 2021.
- 545 Hilker, T., Wulder, M. A., Coops, N. C., Linke, J., McDermid, G., Masek, J. G., Gao, F., and White, J. C.: A new data fusion model for high spatial- and temporal-resolution mapping of forest disturbance based on Landsat and MODIS, Remote Sensing of Environment, 113, 1613–1627, 10.1016/j.rse.2009.03.007, 2009.
- Hoekstra, M., Jiang, M., Clausi, D. A., and Duguay, C.: Lake Ice-Water Classification of RADARSAT-2 Images by Integrating IRGS Segmentation with Pixel-Based Random Forest Labeling, Remote Sensing, 12, 10.3390/rs12091425, 2020.
- 550 Howell, S. E. L., Brown, L. C., Kang, K. K., and Duguay, C. R.: Variability in ice phenology on Great Bear Lake and Great Slave Lake, Northwest Territories, Canada, from SeaWinds/QuikSCAT: 2000–2006, Remote Sensing of Environment, 113, 816–834, 10.1016/j.rse.2008.12.007, 2009.
- IPCC: Climate Change 2021: The Physical Science Basis., Contribution of Working Group I to the Sixth Assessment Report of the Intergovernmental Panel on Climate Change, 2021.
- 555 Jarihani, A., McVicar, T., Van Niel, T., Emelyanova, I., Callow, J., and Johansen, K.: Blending Landsat and MODIS Data to Generate Multispectral Indices: A Comparison of “Index then Blend” and “Blend then Index” Approaches, Remote Sensing, 6, 9213–9238, 10.3390/rs6109213, 2014.
- Jeffries, M. O., Morris, K., and Kozlenko, N.: Ice Characteristics and Processes, and Remote Sensing of Frozen Rivers and Lakes, in: Remote Sensing in Northern Hydrology: Measuring Environmental Change, edited by: Pietroniro, C. R. D. A., 10.1029/GM163, 2013.
- 560 Kang, K. K., Duguay, C. R., Lemmetyinen, J., and Gel, Y.: Estimation of ice thickness on large northern lakes from AMSR-E brightness-temperature measurements, Remote sensing of environment, 150, 1–19, 2014.
- Kawamura, T., Ozeki, T., Wakabayashi, H., and Koarai, M.: Unusual lake ice phenomena observed in Lake Inawashiro, Japan: spray ice and ice balls, Journal of Glaciology, 55, 939–942, 10.3189/002214309790152500, 2009.
- 565 Ke, C.-Q., Tao, A.-Q., and Jin, X.: Variability in the ice phenology of Nam Co Lake in central Tibet from scanning multichannel microwave radiometer and special sensor microwave/imager: 1978 to 2013, Journal of Applied Remote Sensing, 7, 10.1117/4.Jrs.7.073477, 2013.
- Knauer, K., Gessner, U., Fensholt, R., and Kuenzer, C.: An ESTARFM Fusion Framework for the Generation of Large-Scale Time Series in Cloud-Prone and Heterogeneous Landscapes, Remote Sensing, 8, 10.3390/rs8050425, 2016.
- 570 Lang, J., Lyu, S., Li, Z., Ma, Y., and Su, D.: An Investigation of Ice Surface Albedo and Its Influence on the High-Altitude Lakes of the Tibetan Plateau, Remote Sensing, 10, 10.3390/rs10020218, 2018.
- Langlois, T. H.: The Waves of Lake Erie at South Bass Island.

- Leppäranta, M.: Freezing of lakes and the evolution of their ice cover, Springer Science & Business Media, 10.1007/978-3-642-29081-7, 2015.
- 575 Li, W., Lu, P., Li, Z., Zhuang, F., Lu, Z., and Li, G. Y.: Analysis of ice cracks morphology on lake surface of Lake Wuliangsuhai in the winter of 2017-2018, *Journal of Glaciology and Geocryology*, 42, 919-926, 2020.
- Li, Z., Ao, Y., Lyu, S., Lang, J., Wen, L., Stepanenko, V., Meng, X., and Zhao, L. I. N.: Investigation of the ice surface albedo in the Tibetan Plateau lakes based on the field observation and MODIS products, *Journal of Glaciology*, 64, 506-516, 10.1017/jog.2018.35, 2018.
- 580 Liu, C., Duan, P., Zhang, F., Jim, C. Y., Tan, M. L., and Chan, N. W.: Feasibility of the Spatiotemporal Fusion Model in Monitoring Ebinur Lake's Suspended Particulate Matter under the Missing Data Scenario, *Remote Sensing*, 13, 10.3390/rs13193952, 2021.
- Liu, M., Liu, X., Wu, L., Zou, X., Jiang, T., and Zhao, B.: A Modified Spatiotemporal Fusion Algorithm Using Phenological Information for Predicting Reflectance of Paddy Rice in Southern China, *Remote Sensing*, 10, 10.3390/rs10050772, 2018.
- 585 Liu, X., Zhang, G., Sun, G., Wu, Y., and Chen, Y.: Assessment of Lake Water Quality and Eutrophication Risk in an Agricultural Irrigation Area: A Case Study of the Chagan Lake in Northeast China, *Water*, 11, 10.3390/w11112380, 2019.
- Liu, X., Zhang, G., Zhang, J., Xu, Y. J., Wu, Y., Wu, Y., Sun, G., Chen, Y., and Ma, H.: Effects of Irrigation Discharge on Salinity of a Large Freshwater Lake: A Case Study in Chagan Lake, Northeast China, *Water*, 12, 10.3390/w12082112, 2020.
- 590 Loewe, F.: An Observation of "Ball Ice", *Journal of Glaciology*, 1, 340-340, 10.3189/S0022143000010169, 1949.
- Lu, Y., Wu, P., Ma, X., and Li, X.: Detection and prediction of land use/land cover change using spatiotemporal data fusion and the Cellular Automata-Markov model, *Environmental Monitoring and Assessment*, 191, 10.1007/s10661-019-7200-2, 2019.
- Magnuson, J. J., Robertson, D. M., Benson, B. J., Wynne, R. H., Livingstone, D. M., Arai, T., Assel, R. A., Barry, R. G., Card, V., Kuusisto, E., Granin, N. G., Prowse, T. D., Stewart, K. M., and Vuglinski, V. S.: Historical trends in lake and river ice cover in the Northern Hemisphere, *Science*, 289, 1743-1746, 10.1126/science.289.5485.1743, 2000.
- 595 Murfitt, J. and Duguay, C. R.: Assessing the Performance of Methods for Monitoring Ice Phenology of the World's Largest High Arctic Lake Using High-Density Time Series Analysis of Sentinel-1 Data, *Remote Sensing*, 12, 10.3390/rs12030382, 2020.
- Murfitt, J. and Duguay, C. R.: 50 years of lake ice research from active microwave remote sensing: Progress and prospects, *Remote Sensing of Environment*, 264, 10.1016/j.rse.2021.112616, 2021.
- 600 Murfitt, J., Brown, L. C., and Howell, S. E. L.: Evaluating RADARSAT-2 for the Monitoring of Lake Ice Phenology Events in Mid-Latitudes, *Remote Sensing*, 10, 10.3390/rs10101641, 2018a.
- Murfitt, J. C., Brown, L. C., and Howell, S. E.: Estimating lake ice thickness in Central Ontario, *Plos one*, 13, e0208519, 2018b.
- 605 Qi, M., Liu, S., Yao, X., Xie, F., and Gao, Y.: Monitoring the Ice Phenology of Qinghai Lake from 1980 to 2018 Using Multisource Remote Sensing Data and Google Earth Engine, *Remote Sensing*, 12, 10.3390/rs12142217, 2020.
- Qiu, Y., Wang, X., Ruan, Y., Xie, P., Zhong, Y., and Yang, S.: Passive microwave remote sensing of lake freeze-thawing over Qinghai-Tibet Plateau, *Journal of Lake Sciences*, 30, 1438-1449, 2018.
- Ryu, J. H. and Ishizaka, J.: GOCI data processing and ocean applications, *Ocean Science Journal*, 47, 221-221, 10.1007/s12601-012-0023-5, 2012.
- 610 Ryu, J. H., Han, H. J., Cho, S., Park, Y. J., and Ahn, Y. H.: Overview of geostationary ocean color imager (GOCI) and GOCI data processing system (GDPS), *Ocean Science Journal*, 47, 223-233, 10.1007/s12601-012-0024-4, 2012.
- Sisheber, B., Marshall, M., Mengistu, D., and Nelson, A.: Tracking crop phenology in a highly dynamic landscape with knowledge-based Landsat-MODIS data fusion, *International Journal of Applied Earth Observation and Geoinformation*, 106, 10.1016/j.jag.2021.102670, 2022.
- 615 Song, K., Wang, M., Du, J., Yuan, Y., Ma, J., Wang, M., and Mu, G.: Spatiotemporal Variations of Lake Surface Temperature across the Tibetan Plateau Using MODIS LST Product, *Remote Sensing*, 8, 10.3390/rs8100854, 2016.
- Song, K., Wang, Z., Blackwell, J., Zhang, B., Li, F., Zhang, Y., and Jiang, G.: Water quality monitoring using Landsat Thematic Mapper data with empirical algorithms in Chagan Lake, China, *Journal of Applied Remote Sensing*, 5, 3506, 10.1117/1.3559497, 2011.
- 620 SROCC, I.: IPCC Special Report on the Ocean and Cryosphere in a Changing Climate Cambridge University Press, Cambridge, UK and New York, NY, USA, 10.1017/9781009157964, 2019.
- Tom, M., Aguilar, R., Imhof, P., Leinss, S., Baltasvias, E., and Schindler, K.: Lake Ice Detection from Sentinel-1 SAR with

Deep Learning, arXiv preprint arXiv:07040, 2020.

- 625 Wang, X., Feng, L., Gibson, L., Qi, W., Liu, J., Zheng, Y., Tang, J., Zeng, Z., and Zheng, C.: High Resolution Mapping of Ice Cover Changes in Over 33,000 Lakes Across the North Temperate Zone, 48, e2021GL095614, <https://doi.org/10.1029/2021GL095614>, 2021a.
- Wang, Y., Xie, D., Zhan, Y., Li, H., Yan, G., and Chen, Y.: Assessing the Accuracy of Landsat-MODIS NDVI Fusion with Limited Input Data: A Strategy for Base Data Selection, *Remote Sensing*, 13, 10.3390/rs13020266, 2021b.
- 630 Weber, H., Riffler, M., Noges, T., and Wunderle, S.: Lake ice phenology from AVHRR data for European lakes: An automated two-step extraction method, *Remote Sensing of Environment*, 174, 329-340, 10.1016/j.rse.2015.12.014, 2016.
- Wen, Z., Song, K., Shang, Y., Lyu, L., Yang, Q., Fang, C., Du, J., Li, S., Liu, G., Zhang, B., and Cheng, S.: Variability of chlorophyll and the influence factors during winter in seasonally ice-covered lakes, *J Environ Manage*, 276, 111338, 10.1016/j.jenvman.2020.111338, 2020.
- 635 Xie, F., Lu, P., Cheng, B., Yang, Q., and Li, Z.: Magialc shpereical ice (ice balls, ice eggs), *Journal of lake sciences*, 695-698, 2022(in Chinese).
- Xie, P., Qiu, Y., Wang, X., Shi, L., and Liang, W.: Lake Ice Phenology Extraction using Machine Learning Methodology, 2020.
- Yang, Q., Song, K. S., Wen, Z. D., Hao, X. H., and Fang, C.: Recent trends of ice phenology for eight large lakes using MODIS products in Northeast China, *International Journal of Remote Sensing*, 40, 5388-5410, 10.1080/01431161.2019.1579939, 2019.
- 640 Yang, X., Pavelsky, T. M., and Allen, G. H.: The past and future of global river ice, *Nature*, 577, 69-73, 10.1038/s41586-019-1848-1, 2020.
- Zhang, X., Wang, K., and Kirillin, G.: An Automatic Method to Detect Lake Ice Phenology Using MODIS Daily Temperature Imagery, *Remote Sensing*, 13, 10.3390/rs13142711, 2021.
- Zhu, X., Chen, J., Gao, F., Chen, X., and Masek, J. G.: An enhanced spatial and temporal adaptive reflectance fusion model for complex heterogeneous regions, *Remote Sensing of Environment*, 114, 2610-2623, 10.1016/j.rse.2010.05.032, 2010.
- 645 Zhu, X., Helmer, E. H., Gao, F., Liu, D., Chen, J., and Lefsky, M. A.: A flexible spatiotemporal method for fusing satellite images with different resolutions, *Remote Sensing of Environment*, 172, 165-177, 10.1016/j.rse.2015.11.016, 2016.
- Arp, C. D., Cherry, J. E., Brown, D., Bondurant, A. C., and Endres, K. L.: Observation-derived ice growth curves show patterns and trends in maximum ice thickness and safe travel duration of Alaskan lakes and rivers, *The Cryosphere*, 1-35, 2020.
- Bai, L., Cai, J., Liu, Y., Chen, H., Zhang, B., and Huang, L.: Responses of field evapotranspiration to the changes of cropping pattern and groundwater depth in large irrigation district of Yellow River basin, *Agr. Water. Manage.*, 188, 1-11, 10.1016/j.agwat.2017.03.028, 2017.
- 650 Bojinski, S., Verstraete, M., Peterson, T. C., Richter, C., Simmons, A., and Zemp, M.: The concept of essential climate variables in support of climate research, applications, and policy, *B. Am. Meteorol. Soc.*, 95, 1431-1443, 10.1175/bams-d-13-00047.1, 2014.
- 655 Brown, L. C. and Duguay, C. R.: The response and role of ice cover in lake-climate interactions, *Prog. Phys. Geog.*, 34, 671-704, 10.1177/0309133310375653, 2010.
- Cai, Y., Ke, C. Q., and Duan, Z.: Monitoring ice variations in Qinghai Lake from 1979 to 2016 using passive microwave remote sensing data, *Sci. Total Environ.*, 607, 120-131, 10.1016/j.scitotenv.2017.07.027, 2017.
- Cai, Y., Ke, C. Q., Li, X., Zhang, G., Duan, Z., and Lee, H.: Variations of lake ice phenology on the Tibetan Plateau from 2001 to 2017 based on MODIS data, *J. Geophys. Res-Atmos.*, 124, 825-843, 10.1029/2018jd028993, 2019.
- 660 Canny, J.: A computational approach to edge detection, *IEEE T. Pattern Anal.*, 8, 679-698, 1986.
- Dierking, W.: Mapping of different sea ice regimes using images from Sentinel-1 and ALOS synthetic aperture radar, *IEEE T. Geosci. Remote.*, 48, 1045-1058, 10.1109/TGRS.2009.2031806, 2010.

- 665 [Doernhoefer, K. and Oppelt, N.: Remote sensing for lake research and monitoring - Recent advances. \*Ecol. Indic.\*, 64, 105-122, 10.1016/j.ecolind.2015.12.009, 2016.](#)
- [Du, J., Kimball, J. S., Duguay, C., Kim, Y., and Watts, J. D.: Satellite microwave assessment of Northern Hemisphere lake ice phenology from 2002 to 2015. \*The Cryosphere\*, 11, 47-63, 10.5194/tc-11-47-2017, 2017.](#)
- [Du, J., Watts, J. D., Jiang, L., Lu, H., Cheng, X., Duguay, C., Farina, M., Qiu, Y., Kim, Y., Kimball, J. S., and Tarolli, P.: Remote sensing of environmental changes in cold regions: Methods, achievements and challenges. \*Remote. Sens.\*, 11, 10.3390/rs11161952, 2019.](#)
- 670 [Duan, H., Zhang, Y., Zhang, B., Song, K., and Wang, Z.: Assessment of chlorophyll-a concentration and trophic state for Lake Chagan using Landsat TM and field spectral data. \*Environ. Monit. Assess.\*, 129, 295-308, 10.1007/s10661-006-9362-y, 2007.](#)
- [Feng, G., Masek, J., Schwaller, M., and Hall, F.: On the blending of the Landsat and MODIS surface reflectance: predicting daily Landsat surface reflectance. \*IEEE T. Geosci. Remote.\*, 44, 2207-2218, 10.1109/tgrs.2006.872081, 2006.](#)
- 675 [Geldsetzer, T., Sanden, J. v. d., and Brisco, B.: Monitoring lake ice during spring melt using RADARSAT-2 SAR. \*Can. J. Remote Sens.\*, 36, S391-S400, 2010.](#)
- [Gogineni, P. and Yan, J.-B.: Remote sensing of ice thickness and surface velocity, in: \*Remote Sensing of the Cryosphere\*, edited by: Tedesco, M., John Wiley & Sons, Ltd., 2015.](#)
- [Gusmeroli, A. and Grosse, G.: Ground penetrating radar detection of subsnow slush on ice-covered lakes in interior Alaska. \*The Cryosphere\*, 6, 1435-1443, 10.5194/tc-6-1435-2012, 2012.](#)
- 680 [Hampton, S. E., Galloway, A. W., Powers, S. M., Ozersky, T., Woo, K. H., Batt, R. D., Labou, S. G., O'Reilly, C. M., Sharma, S., Lottig, N. R., Stanley, E. H., North, R. L., Stockwell, J. D., Adrian, R., Weyhenmeyer, G. A., Arvola, L., Baulch, H. M., Bertani, I., Bowman, L. L., Jr., Carey, C. C., Catalan, J., Colom-Montero, W., Domine, L. M., Filip, M., Granados, I., Gries, C., Grossart, H. P., Haberman, J., Haldna, M., Hayden, B., Higgins, S. N., Jolley, J. C., Kahilainen, K. K., Kaup, E., Kehoe,](#)
- 685 [M. J., MacIntyre, S., Mackay, A. W., Mariash, H. L., McKay, R. M., Nixdorf, B., Noges, P., Noges, T., Palmer, M., Pierson, D. C., Post, D. M., Pruett, M. J., Rautio, M., Read, J. S., Roberts, S. L., Rucker, J., Sadro, S., Silow, E. A., Smith, D. E., Sterner, R. W., Swann, G. E., Timofeyev, M. A., Toro, M., Twiss, M. R., Vogt, R. J., Watson, S. B., Whiteford, E. J., and Xenopoulos, M. A.: Ecology under lake ice. \*Ecol. Lett.\*, 20, 98-111, 10.1111/ele.12699, 2017.](#)
- [Hao, X., Yang, Q., Shi, X., Liu, X., Huang, W., Chen, L., and Ma, Y.: Fractal-based retrieval and potential driving factors of lake ice fractures of Chagan Lake, Northeast China using Landsat remote sensing images. \*Remote Sens.\*, 13, 10.3390/rs13214233, 2021.](#)
- 690 [Hilker, T., Wulder, M. A., Coops, N. C., Linke, J., McDermid, G., Masek, J. G., Gao, F., and White, J. C.: A new data fusion model for high spatial- and temporal-resolution mapping of forest disturbance based on Landsat and MODIS. \*Remote Sens. Environ.\*, 113, 1613-1627, 10.1016/j.rse.2009.03.007, 2009.](#)
- 695 [Hoekstra, M., Jiang, M., Clausi, D. A., and Duguay, C.: Lake ice-water classification of RADARSAT-2 images by integrating IRGS Segmentation with pixel-based random forest labeling. \*Remote Sens.\*, 12, 10.3390/rs12091425, 2020.](#)

- Howell, S. E. L., Brown, L. C., Kang, K.-K., and Duguay, C. R.: Variability in ice phenology on Great Bear Lake and Great Slave Lake, Northwest Territories, Canada, from SeaWinds/QuikSCAT: 2000-2006, *Remote Sens. Environ.*, 113, 816-834, [10.1016/j.rse.2008.12.007](https://doi.org/10.1016/j.rse.2008.12.007), 2009.
- 700 [IPCC: Climate change 2021: The physical science basis., Contribution of Working Group I to the Sixth Assessment Report of the Intergovernmental Panel on Climate Change, 2021.](#)
- [Jarihani, A., McVicar, T., Van Niel, T., Emelyanova, I., Callow, J., and Johansen, K.: Blending Landsat and MODIS data to generate multispectral indices: A comparison of “Index-then-Blend” and “Blend-then-Index” approaches, \*Remote Sens.\*, 6, 9213-9238, \[10.3390/rs6109213\]\(https://doi.org/10.3390/rs6109213\), 2014.](#)
- 705 [Jeffries, M. O., Morris, K., and Kozlenko, N.: Ice characteristics and processes, and remote sensing of frozen rivers and lakes, in: \*Remote Sensing in Northern Hydrology: Measuring Environmental Change\*, edited by: Pietroniro, C. R. D. A., \[10.1029/GM163\]\(https://doi.org/10.1029/GM163\), 2013.](#)
- [Kang, K.-K. K., Duguay, C. R., Lemmetyinen, J., and Gel, Y.: Estimation of ice thickness on large northern lakes from AMSR-E brightness temperature measurements, \*Remote Sens. Environ.\*, 150, 1-19, 2014.](#)
- 710 [Ke, C.-Q., Tao, A.-Q., and Jin, X.: Variability in the ice phenology of Nam Co Lake in central Tibet from scanning multichannel microwave radiometer and special sensor microwave/imager: 1978 to 2013, \*J. Appl. Remote. Sens.\*, 7, \[10.1117/1.Jrs.7.073477\]\(https://doi.org/10.1117/1.Jrs.7.073477\), 2013.](#)
- [Knauer, K., Gessner, U., Fensholt, R., and Kuenzer, C.: An ESTARFM fusion framework for the generation of large-scale time series in cloud-prone and heterogeneous landscapes, \*Remote. Sens.\*, 8, \[10.3390/rs8050425\]\(https://doi.org/10.3390/rs8050425\), 2016.](#)
- 715 [Lang, J., Lyu, S., Li, Z., Ma, Y., and Su, D.: An investigation of ice surface albedo and its influence on the high-altitude lakes of the Tibetan Plateau, \*Remote. Sens.\*, 10, \[10.3390/rs10020218\]\(https://doi.org/10.3390/rs10020218\), 2018.](#)
- [Leppäranta, M.: Modelling the formation and decay of lake ice, in: \*The Impact of Climate Change on European Lakes\*, edited by: George, G., Springer Netherlands, Dordrecht, 63-83, \[10.1007/978-90-481-2945-4\\\_5\]\(https://doi.org/10.1007/978-90-481-2945-4\_5\), 2010.](#)
- [Leppäranta, M.: Freezing of lakes and the evolution of their ice cover, Springer Science & Business Media, \[10.1007/978-3-642-29081-7\]\(https://doi.org/10.1007/978-3-642-29081-7\), 2015.](#)
- 720 [Li, W., Lu, P., Li, Z., Zhuang, F., Lu, Z., and Li, G.: Analysis of ice cracks morphology on lake surface of Lake Wuliangsu Hai in the winter of 2017-2018, \*J. Glaciol. Geocry.\*, 42, 919-926, 2020, \[10.7522/j.issn.1000-0240.2020.0066\]\(https://doi.org/10.7522/j.issn.1000-0240.2020.0066\). \(in Chinese\)](#)
- [Li, Z., Ao, Y., Lyu, S., Lang, J., Wen, L., Stepanenko, V., Meng, X., and Zhao, L. I. N.: Investigation of the ice surface albedo in the Tibetan Plateau lakes based on the field observation and MODIS products, \*J. Glaciol.\*, 64, 506-516, \[10.1017/jog.2018.35\]\(https://doi.org/10.1017/jog.2018.35\),](#)
- 725 [2018.](#)
- [Liu, C., Duan, P., Zhang, F., Jim, C.-Y., Tan, M. L., and Chan, N. W.: Feasibility of the spatiotemporal fusion model in monitoring Ebinur Lake’s suspended particulate matter under the missing-data scenario, \*Remote Sens.\*, 13, \[10.3390/rs13193952\]\(https://doi.org/10.3390/rs13193952\), 2021.](#)
- [Liu, M., Liu, X., Wu, L., Zou, X., Jiang, T., and Zhao, B.: A modified spatiotemporal fusion algorithm using phenological information for predicting reflectance of paddy Rice in Southern China, \*Remote Sens.\*, 10, \[10.3390/rs10050772\]\(https://doi.org/10.3390/rs10050772\), 2018a.](#)
- 730

- Liu, X., Li, B., Li, Z., and Shen, W.: A new fracture model for reservoir ice layers in the northeast cold region of China. *Constr. Build. Mater.*, 191, 795-811, [10.1016/j.conbuildmat.2018.10.050](https://doi.org/10.1016/j.conbuildmat.2018.10.050), 2018b.
- Liu, X., Zhang, G., Sun, G., Wu, Y., and Chen, Y.: Assessment of Lake water quality and eutrophication risk in an agricultural irrigation area: A case study of the Chagan Lake in Northeast China. *Water*, 11, [10.3390/w11112380](https://doi.org/10.3390/w11112380), 2019.
- 735 Liu, X., Zhang, G., Zhang, J., Xu, Y. J., Wu, Y., Wu, Y., Sun, G., Chen, Y., and Ma, H.: Effects of irrigation discharge on salinity of a large freshwater lake: A case study in Chagan Lake, Northeast China. *Water*, 12, [10.3390/w12082112](https://doi.org/10.3390/w12082112), 2020.
- Lu, Y., Wu, P., Ma, X., and Li, X.: Detection and prediction of land use/land cover change using spatiotemporal data fusion and the Cellular Automata–Markov model. *Environ. Monit. Assess.*, 191, [10.1007/s10661-019-7200-2](https://doi.org/10.1007/s10661-019-7200-2), 2019.
- Magnuson, J. J., Robertson, D. M., Benson, B. J., Wynne, R. H., Livingstone, D. M., Arai, T., Assel, R. A., Barry, R. G., Card, V., Kuusisto, E., Granin, N. G., Prowse, T. D., Stewart, K. M., and Vuglinski, V. S.: Historical trends in lake and river ice cover in the Northern Hemisphere. *Science*, 289, 1743-1746, [10.1126/science.289.5485.1743](https://doi.org/10.1126/science.289.5485.1743), 2000.
- 740 Murfitt, J. and Duguay, C. R.: Assessing the performance of methods for monitoring ice phenology of the world's largest high Arctic lake using high-density time series analysis of Sentinel-1 data. *Remote Sens.*, 12, [10.3390/rs12030382](https://doi.org/10.3390/rs12030382), 2020.
- Murfitt, J. and Duguay, C. R.: 50 years of lake ice research from active microwave remote sensing: Progress and prospects. *Remote Sens. Environ.*, 264, [10.1016/j.rse.2021.112616](https://doi.org/10.1016/j.rse.2021.112616), 2021.
- 745 Murfitt, J., Brown, L. C., and Howell, S. E. L.: Evaluating RADARSAT-2 for the monitoring of lake ice phenology events in mid-latitudes. *Remote Sens.*, 10, [10.3390/rs10101641](https://doi.org/10.3390/rs10101641), 2018a.
- Murfitt, J. C., Brown, L. C., and Howell, S. E.: Estimating lake ice thickness in Central Ontario. *Plos one*, 13, e0208519, 2018b.
- Qi, M., Liu, S., Yao, X., Xie, F., and Gao, Y.: Monitoring the ice phenology of Qinghai Lake from 1980 to 2018 using multisource remote sensing data and Google Earth Engine. *Remote Sens.*, 12, [10.3390/rs12142217](https://doi.org/10.3390/rs12142217), 2020.
- 750 Qiu, Y., Wang, X., Ruan, Y., Xie, P., Zhong, Y., and Yang, S.: Passive microwave remote sensing of lake freeze-thawing over Qinghai-Tibet Plateau. *J. Lake. Sci.*, 30, 1438-1449, 2018 (in Chinese).
- Ryu, J. H. and Ishizaka, J.: GOCI data processing and ocean applications. *Ocean. Sci. J.*, 47, 221-221, [10.1007/s12601-012-0023-5](https://doi.org/10.1007/s12601-012-0023-5), 2012.
- 755 Ryu, J. H., Han, H. J., Cho, S., Park, Y. J., and Ahn, Y. H.: Overview of geostationary ocean color imager (GOCI) and GOCI data processing system (GDPS). *Ocean. Sci. J.*, 47, 223-233, [10.1007/s12601-012-0024-4](https://doi.org/10.1007/s12601-012-0024-4), 2012.
- Sisheber, B., Marshall, M., Mengistu, D., and Nelson, A.: Tracking crop phenology in a highly dynamic landscape with knowledge-based Landsat–MODIS data fusion. *Int. J. Appl. Earth. Obs.*, 106, [10.1016/j.jag.2021.102670](https://doi.org/10.1016/j.jag.2021.102670), 2022.
- Song, K., Wang, M., Du, J., Yuan, Y., Ma, J., Wang, M., and Mu, G.: Spatiotemporal variations of lake surface temperature across the Tibetan Plateau using MODIS LST product. *Remote. Sens.*, 8, [10.3390/rs8100854](https://doi.org/10.3390/rs8100854), 2016.
- 760 Song, K., Wang, Z., Blackwell, J., Zhang, B., Li, F., Zhang, Y., and Jiang, G.: Water quality monitoring using Landsat Thematic Mapper data with empirical algorithms in Chagan Lake, China. *J. Appl. Remote. Sens.*, 5, 3506, [10.1117/1.3559497](https://doi.org/10.1117/1.3559497), 2011.
- SROCC, I.: IPCC special report on the ocean and cryosphere in a changing climate Cambridge University Press, Cambridge, UK and New York, NY, USA, [10.1017/9781009157964](https://doi.org/10.1017/9781009157964), 2019.



- 765 [Tan, B., Li, Z.-j., Lu, P., Haas, C., and Nicolaus, M.: Morphology of sea ice pressure ridges in the northwestern Weddell Sea in winter, \*J. Geophys. Res-Oceans.\*, 117, n/a-n/a, 10.1029/2011jc007800, 2012.](#)
- [Tom, M., Aguilar, R., Imhof, P., Leinss, S., Baltasvias, E., and Schindler, K.: Lake ice detection from Sentinel-1 SAR with deep learning, \*arXiv preprint arXiv:07040\*, 2020.](#)
- [Wang, K., Leppäranta, M., and Reinart, A.: Modeling ice dynamics in Lake Peipsi, \*JournalVerhandlungen der Internationalen Vereinigung für theoretische und angewandte Limnologie\*, 29, 1443-1446, 2006.](#)
- 770 [Wang, X., Feng, L., Gibson, L., Qi, W., Liu, J., Zheng, Y., Tang, J., Zeng, Z., and Zheng, C.: High-resolution mapping of ice cover changes in over 33,000 lakes across the North Temperate Zone, \*Geophys. Res. Lett.\*, 48, e2021GL095614, <https://doi.org/10.1029/2021GL095614>, 2021a.](#)
- [Wang, Y., Xie, D., Zhan, Y., Li, H., Yan, G., and Chen, Y.: Assessing the accuracy of Landsat-MODIS NDVI fusion with limited input data: A strategy for base data selection, \*Remote. Sens.\*, 13, 10.3390/rs13020266, 2021b.](#)
- 775 [Weber, H., Riffler, M., Noges, T., and Wunderle, S.: Lake ice phenology from AVHRR data for European lakes: An automated two-step extraction method, \*Remote Sens Environ.\*, 174, 329-340, 10.1016/j.rse.2015.12.014, 2016.](#)
- [Wen, Z., Song, K., Shang, Y., Lyu, L., Yang, Q., Fang, C., Du, J., Li, S., Liu, G., Zhang, B., and Cheng, S.: Variability of chlorophyll and the influence factors during winter in seasonally ice-covered lakes, \*J. Environ. Manage.\*, 276, 111338, 10.1016/j.jenvman.2020.111338, 2020.](#)
- 780 [Xie, P., Qiu, Y., Wang, X., Shi, L., and Liang, W.: Lake ice phenology extraction using machine learning methodology, 2020.](#)
- [Yang, Q., Song, K. S., Wen, Z. D., Hao, X. H., and Fang, C.: Recent trends of ice phenology for eight large lakes using MODIS products in Northeast China, \*Int. J. Remote. Sens.\*, 40, 5388-5410, 10.1080/01431161.2019.1579939, 2019.](#)
- [Yang, X., Pavelsky, T. M., and Allen, G. H.: The past and future of global river ice, \*Nature\*, 577, 69-73, 10.1038/s41586-019-1848-1, 2020.](#)
- 785 [Zhang, X., Wang, K., and Kirillin, G.: An automatic method to detect lake ice phenology using MODIS daily temperature imagery, \*Remote. Sens.\*, 13, 10.3390/rs13142711, 2021.](#)
- [Zhu, X., Chen, J., Gao, F., Chen, X., and Masek, J. G.: An enhanced spatial and temporal adaptive reflectance fusion model for complex heterogeneous regions, \*Remote. Sens. Environ.\*, 114, 2610-2623, 10.1016/j.rse.2010.05.032, 2010.](#)
- 790 [Zhu, X., Helmer, E. H., Gao, F., Liu, D., Chen, J., and Lefsky, M. A.: A flexible spatiotemporal method for fusing satellite images with different resolutions, \*Remote. Sens. Environ.\*, 172, 165-177, 10.1016/j.rse.2015.11.016, 2016.](#)

**Tables**

**Table 1** The comparison of band range between GOCI and Landsat. The selected bands for merging Landsat and GOCI are marked with red.

Band	GOCI		Landsat 8 OLI	
	Band centre (nm)	Bandwidth (nm)	Band centre (nm)	Bandwidth (nm)
Band 1	402-422	20	443-453	20
Band 2	433-453	20	450-515	65
Band 3	480-500	20	525-600	75
Band 4	545-565	20	630-680	50
Band 5	650-670	20	845-885	40
Band 6	675-685	10	1560-1660	100
Band 7	735-755	20	2100-2300	200
Band 8	845-885	40	500-680	180

**Table 2** The usage of GOCI images from November 2018 to March 2019.

Date	Image number	Date	Image number
2018.11.21	4	2019.03.14	4
2018.11.22	8	2019.03.15	6
2018.11.23	7	2019.03.16	8
2018.11.24	0	2019.03.17	8
2018.11.25	8	2019.03.18	8
2018.11.26	0	2019.03.19	0
2018.11.27	7	2019.03.20	0
2018.11.28	8	2019.03.21	0
2018.11.29	8	2019.03.22	4
2018.11.30	7	2019.03.23	4
2019.03.15	8	2019.03.24	7
		<b>Total</b>	<b>796</b>

设置了格式: 字体颜色: 自动设置

格式化表格

设置了格式: 字体: 非加粗, 字体颜色: 自动设置

795

Figures

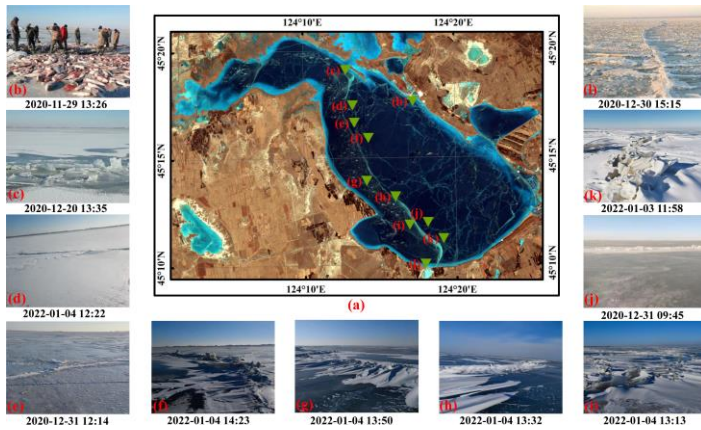
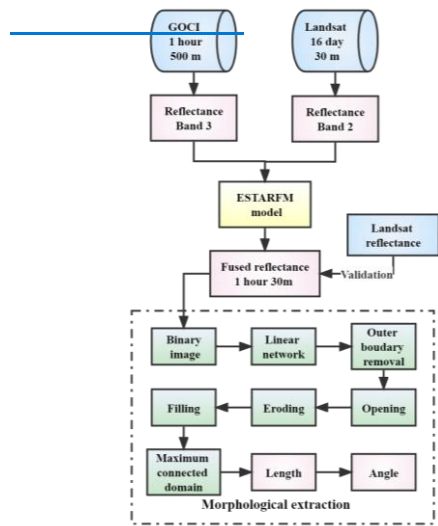
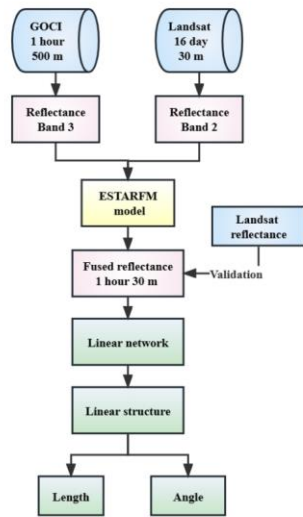


Figure 1 The spatial distribution of Chagan Lake and field photographs. Figure 1 (a) is provided Landsat 8 OLI on February 10, 2019 with the band composite: R(5) + G(4) + B(3). Figure 1 (b) shows the fishing activities of Chagan. Figure 1 (c)-(h) displays the field photographs along the linear structure observed from the satellite images captured in our two recent field investigations.



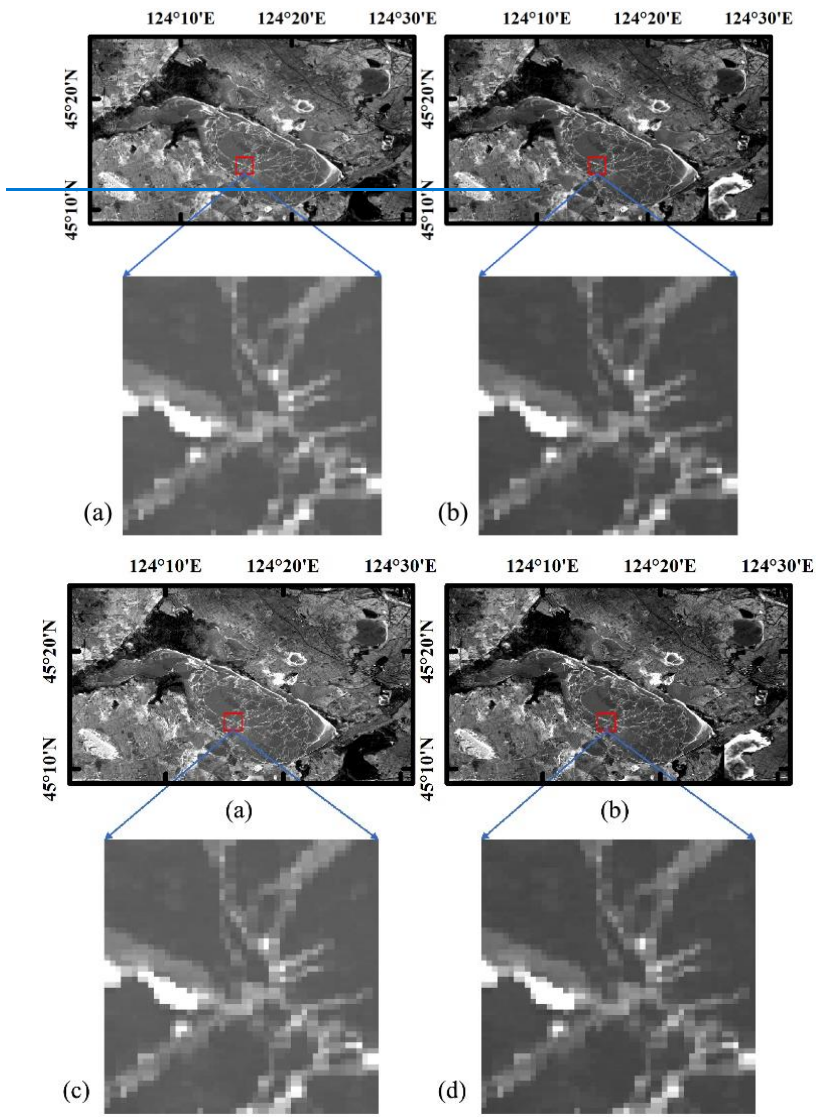
设置了格式: 字体颜色: 自动设置

设置了格式: 字体颜色: 自动设置



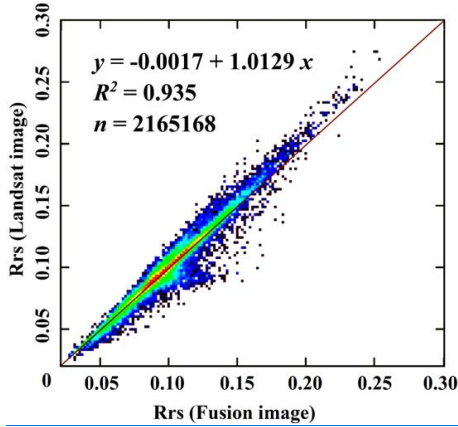
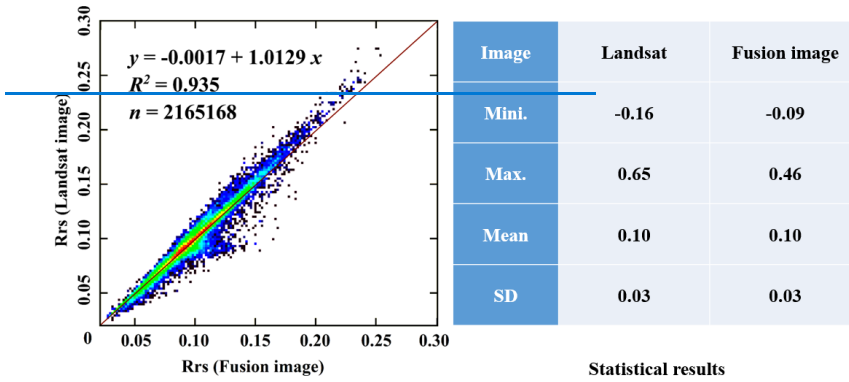
805

Figure 2 The flowchart of the methodology workflow of this study.



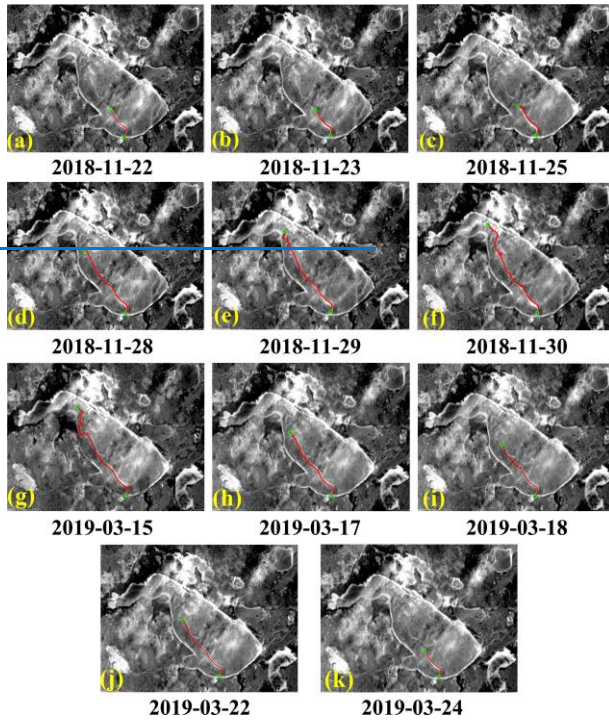
810

Figure 3 The actual image comparison of Landsat 8 OLI (a) and ESTARFM (b) observed on November 22, 2018. (a) and its prediction images by the ESTARFM (b). The lower row images (c) and (d) display the enlargement figure of red rectangle in upper row images (a) and (b).



815

Figure 4 The observed Scatter plot of the real and the predicted reflectance values and estimated value by the ESTARFM for the blue band using ESTARFM. The capture date was November 22, 2018.



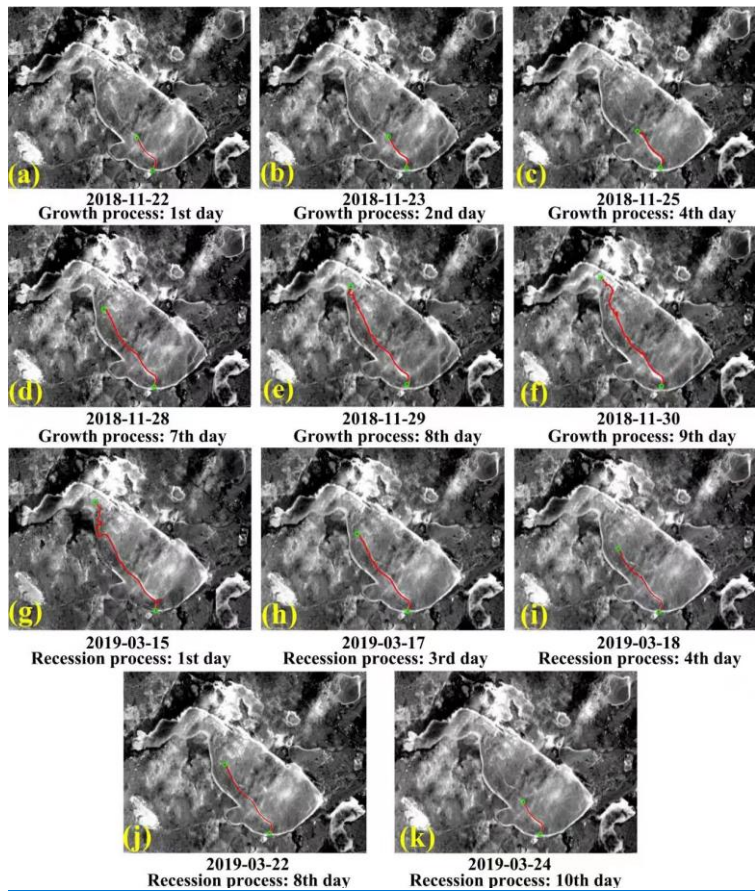
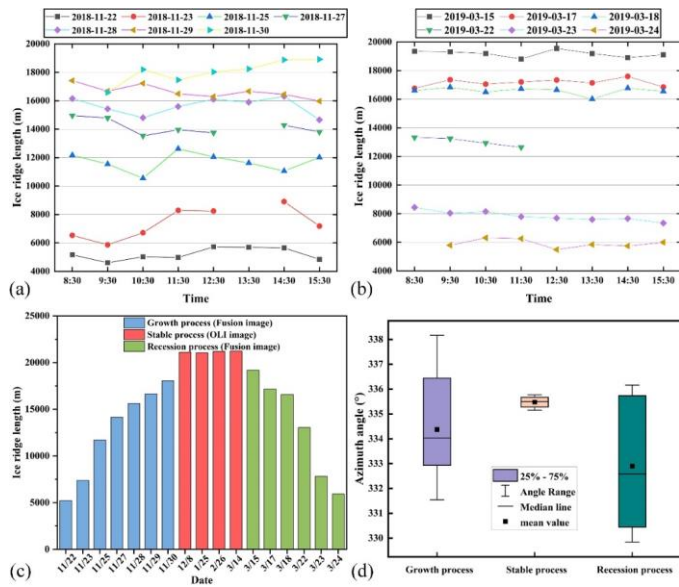


Figure 5 The growthspatial and decay-processtemporal changes of ice ridges derived from the linear structure on fusion data-images of Lake Chagan during the cold season fromof 2018 to 2019.

820





**Figure 56** The changes of ice ridges during the cold season of 2018-2019: (a)-(f) displays length changes during the growth process from November 22, 2018, to November 30, 2018; Figure 5(g)-(k) displays measured from 53 ESTARFM fusion images; (b) length changes during the decay/recession process lasted from March 15 to March 24, 2019, measured from 43 ESTARFM fusion images; (c) the daily average length; (d) the angles of ice ridges in different stages.

825

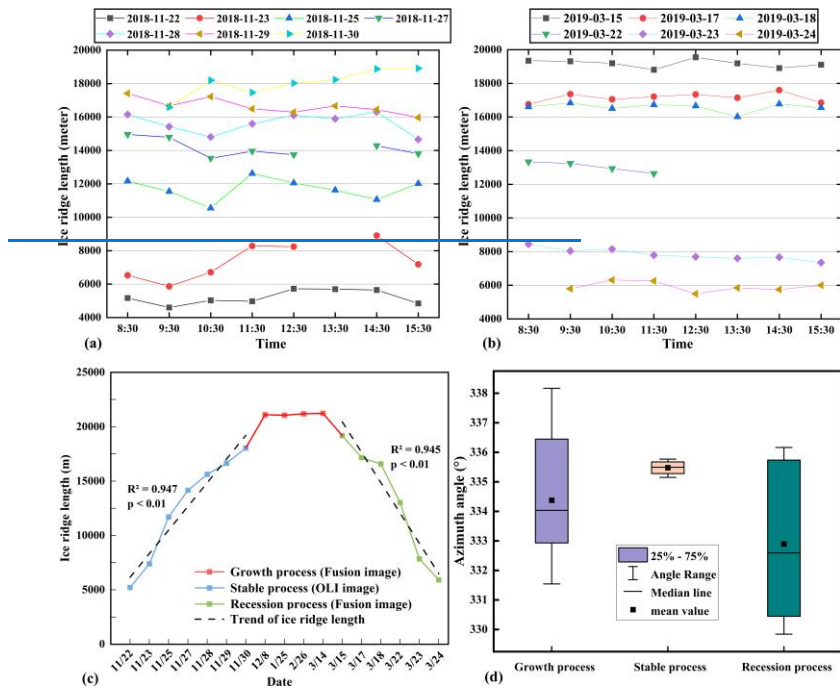
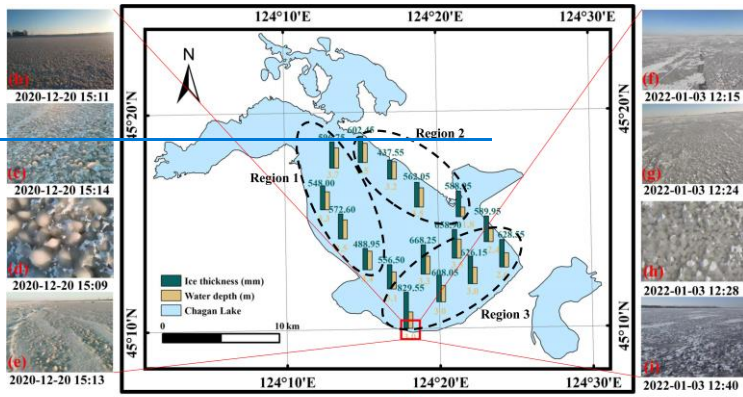
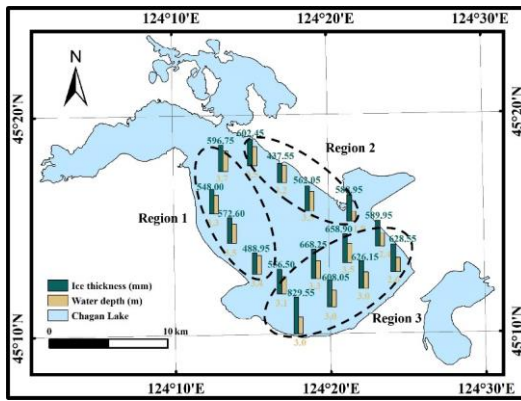


Figure 6 The length changes of ice ridges from November 2018 to March 2019. The length and angle during the growth and recession process were extracted from Landsat-GOCI fusion data, and that of the stable process was extracted from Landsat data.

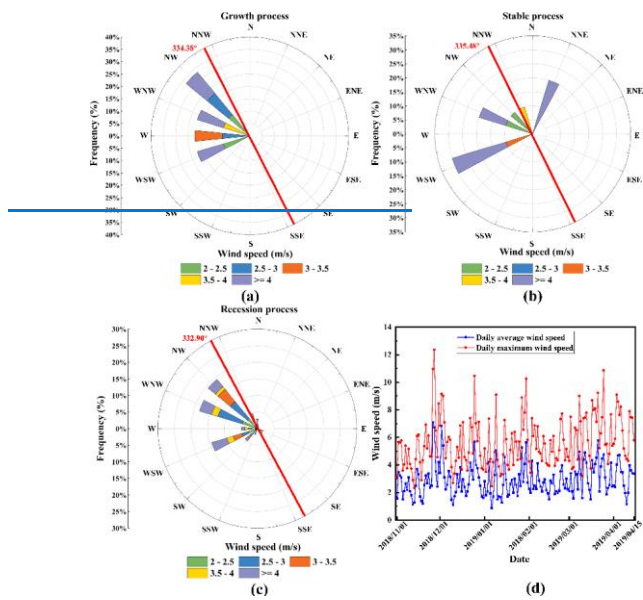


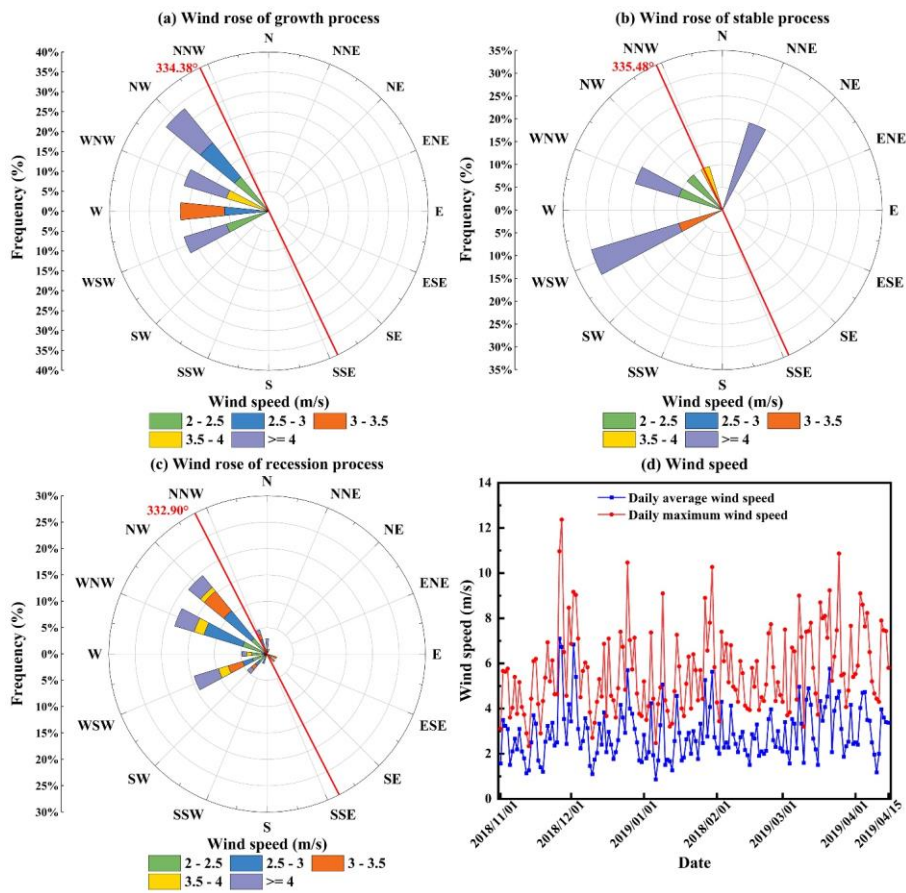
(a)



830

Figure 7 The ice thickness (mm) and water depth (m) of Chagan Lake was measured during the periods from January 2 to 4, 2022, and the field photograph.





835 Figure 8 The wind rosefield of Chagan Lake during the cold season of 2018: (a) growth process from November 22, 2018, to November 30, 2018; (b) stable process; (c) recession process from March 15 to March 24, 2019; (4) daily average and maximum weed speed from November 1, 2018, to April 15, 2019.

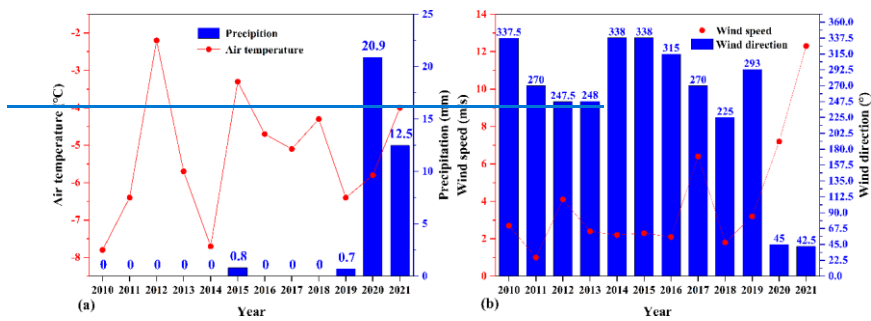


Figure 9 The changes of climate changes around the freeze-up process from 2010 to 2022: (a) air temperature (°C) and precipitation (mm); (b) wind speed (m/s) and wind direction (°). The average values are calculated a week before and after the freeze-up date derived from MODIS.

带格式的: 题注